1 **Programmable downsizing of CRISPR-Cas9 activity for precise and safe genome**

2 **editing**

3

4 **Masaki Kawamata[1]*, Hiroshi I. Suzuki[2,3]*, Ryota Kimura[1], Atsushi Suzuki[1]***

5

6 1. Division of Organogenesis and Regeneration, Medical Institute of Bioregulation,

7   Kyushu University, Fukuoka, Japan.

8 2. Division of Molecular Oncology, Center for Neurological Diseases and Cancer,

9   Nagoya University Graduate School of Medicine, Nagoya, Japan.

10 3. David H. Koch Institute for Integrative Cancer Research, Massachusetts Institute of

11   Technology, Cambridge, MA, USA.

12

13 *Corresponding author: Masaki Kawamata, Hiroshi I. Suzuki, and Atsushi Suzuki

14 Masaki Kawamata, Ph.D. (kawamata@bioreg.kyushu-u.ac.jp)

15 Atsushi Suzuki, Ph.D. (suzukicks@bioreg.kyushu-u.ac.jp)

16 Division of Organogenesis and Regeneration, Medical Institute of Bioregulation, Kyushu

17 University, 3-1-1 Maidashi, Higashi-ku, Fukuoka 812-8582, Japan. Phone: +81-92-642-

18 6449

19 Hiroshi I. Suzuki, M.D., Ph.D. (hisuzuki@med.nagoya-u.ac.jp)

20 Division of Molecular Oncology, Center for Neurological Diseases and Cancer, Nagoya

21 University Graduate School of Medicine, 65 Tsurumai-cho, Showa-ku, Nagoya 466-8550,

22 Japan. Phone: +81-52-741-2111

23

Abstract

24

25 CRSIPR-Cas9 system has opened up the avenue to efficient genome editing[1-4]. However,

26 together with known off-target effects, several concerns of current CRISPR-Cas9 platform,

27 including severe DNA damage, cytotoxicity, and large genomic alteration, have emerged

28 in recent reports[5-7] and establish a formidable obstacle to precisely model allele dosage

29 effects of disease mutations and risk variants, especially mono-allelic effects, and correct

30 them. Here, by developing an allele-specific indel monitor system (AIMS), we demonstrate

31 that small and simple modification of conventional single-guide RNAs (sgRNAs) enable

32 programmable tuning of CRISPR-Cas9 activities and alleviate such adverse effects. AIMS,

33 which visualizes various indel events in two alleles separately in living cells, is convenient

34 and accurate to determine the *in vitro* editing efficiency and revealed frequent mosaicism

35 during genome editing. Using AIMS, we show that adding cytosine stretches to the 5' end

36 of conventional sgRNA efficiently reduced Cas9 activity in a length dependent manner. By

37 combining systematic experiments and computational modeling, we established the

38 quantitative relationships between the length of cytosine extension and multiple aspects of

39 CRISPR-Cas9 system. In general, short cytosine extension dramatically relieves p53-

40 dependent cytotoxicity and suppression of homology-directed repair (HDR) while

41 relatively maintaining on-target activity. Long cytosine extension further decreases on-

42 target activity, thereby maximizing mono-allelic editing, while conventional system

43 typically induces bi-allelic editing. Furthermore, such downregulation of on-target activity

44 contributes to downregulation of relative off-target activity and protection of HDR-allele

45 from second off-target editing. Therefore, cytosine extension method finally enables both

46 single-step   generation   of   heterozygous   single-nucleotide   disease   mutations   from

47   homozygous states in mouse ES cells and correction of heterozygous disease mutations in

48   human iPS cells. Taken together, our study proposes updates of standard CRISPR-Cas9

49   platform in mammalian cells toward precise and safe genome editing in diverse

50   applications.

51

Introduction

CRSIPR-Cas9 system has opened up the avenue to efficient genome editing[1-4]. It is still challenging to model and correct most genetic variants that contribute to various diseases. Several methods such as CORRECT combine the standard CRISPR-Cas9 system and homology-directed repair (HDR) for this purpose[8,9]. However, they typically require introduction of silent mutations in HDR templates to protect the HDR-allele from second editing since the HDR templates are easy targets for off-target activities of Cas9, and multiple cloning steps are thus inevitable to revert silent mutations. Other approaches such as base editing (BE) or prime editing (PE) avoid DNA double-strand break (DSB)[10-13], but still accompany with insertions/deletions (indels) and undesirable mutations caused by editing errors[14-17]. Besides known off-target effects, multiple recent studies have unveiled that several adverse effects, such as cytotoxicity with severe DNA damage, large on-target genomic deletion, and chromosomal rearrangement, are prevalent in mammalian cells[5-7]. Indeed, the large deletions are induced in up to 20% of cells[7]. Among them, the large DNA deletions are particularly underestimated in the next-generation sequencing (NGS)-based methods, which are typically used for development of CRISPR-based technologies, such as CORRECT, BE, and PE, because short read sequencing analyzes only partially matched target sequences. NGS-based methods also miss clonal and allelic editing information, including the prevalence of mosaicism. To investigate an avenue for safe genome editing, we first attempted to establish a convenient but accurate experimental platform to visualize the dynamics of genome editing in each single allele at the single cell level in living cells: allele-specific indel monitor system (AIMS).

75

Results

Allele-specific indel monitor system (AIMS)

78   An allele-specific indel monitor system (AIMS) employs insertion of the monitor cassette

79   containing 2A self-cleaving peptides (P2A) and two distinct fluorescent proteins

80   (tdTomato and Venus) in two alleles (Fig. 1a). Use of sgRNA targeting a P2A sequence

81   allows us to analyze indel induction in a pair of alleles by two distinct colors in real-time

82   and at clonal level without sequence analysis. By inserting AIMS cassette downstream of

83   coding regions of genes, which products localize to the nuclei or cell membrane, e.g.

84   transcription factors (TF) or membrane proteins (MP), changes in localization of two

85   fluorescence can distinguish nine combinations consisting of in-frame indels, frameshift

86   indels or large deletions, and no indel at each allele (Fig. 1a). For example, in-frame indels

87   disrupt endopeptidase recognition of P2A peptides and thus result in change in fluorescence

88   localization to nucleus or membrane. AIMS is also sensitive to large deletions, which cause

89   loss of fluorescence. In AIMS, multiple sgRNAs can be tested using several target sites in

90   P2A sequence and/or generating P2A variants with silent mutations (Fig. 1b). In this study,

91   we used an original P2A sequence, named $P2A_1$[18], and one of its variants, named $P2A_2$,

92   and tested six sgRNAs targeting $P2A_1$ or $P2A_2$ (Fig. 1b). We first developed AIMS in

93   mouse embryonic stem cells (mESCs) by targeting T-Box transcription factor 3 (*Tbx3)* and

94   membrane protein E-cadherin (*Cdh1*) because they are homogenously expressed in mESCs

95   under a 2iL culture condition[19,20] (Extended Data Fig. 1a). AIMS successfully

96   distinguished various combinations and was consistent with sequence validation (Fig. 1c

97   and Extended Data Fig. 1b, c).

98   To enhance experimental reproducibility, we mainly utilized the all-in-one

99   plasmids expressing single-guide RNA (sgRNA), Cas9, and puromycin-resistant cassette

100   (p:RCP), and performed AIMS analysis in cells selected by puromycin treatment (Fig. 1d).

101   Notably, approximately 30 % of primary colonies derived from puromycin-resistant single

102   cells exhibited mosaicism (Fig. 1d). Thus, the primary colonies were dissociated and the

103   secondary ones with homogenous fluorescent pattern were analyzed (Fig. 1d). Bi-allelic

104   indels were induced in more than 99.4% of mESC clones for all of six tested sgRNAs

105   targeting $P2A_1$ or $P2A_2$ (Fig. 1e). Similar results were obtained when endogenous genes

106   were targeted (Fig. 1f). Although the CRISPR editing efficiency is reportedly influenced

107   by chromatin accessibility[21], we confirmed high rates of bi-allelic indels for *Alb* gene, not

108   expressed in mESCs.

109   Next, we investigated the accuracy of AIMS. When analyzing bi-allelic indel

110   clones, allelic bias in both indel induction and frameshift/in-frame indel frequency was not

111   evident (Fig. 1g and Extended Data Fig. 1d). Frequencies of in-frame indels were lower

112   than those of frameshift indels or large deletions. Next, the error rates of AIMS data-based

113   indel probability (AIMS[P]) were investigated by additional sequence analysis of the rare

114   population of the tdTomato$^+$/Venus^{indel} and tdTomato^{indel}/Venus$^+$ heterozygous clones (Fig.

115   1h). The 86% of these ostensibly heterozygous clones were turned to be homozygous,

116   resulting in the error frequency less than 0.3% (Fig. 1h). We next performed a standard

117   T7E1 survey assay with a bacterial cloning process in our experiments, determined indel

118   probability (T7E1-Bac[P]), and estimated the error rates (Fig.1i). Importantly, additional

119   sequence analysis revealed that approximately 8% of indels were not digested by T7E1

120   (Fig.1j), suggesting that AIMS is more accurate than T7E1 assay. Thus, combination of

6

121　T7E1 and sequence analysis was performed hereafter when determining bacterial cloning-

122　based indel probability (Bac[P]). These results collectively suggest that the current

123　CRISPR-Cas9 system basically induces bi-allelic DNA cleavage when appropriate

124　sgRNAs are designed and Cas9-introduced cells are sufficiently selected, and that editing

125　outcomes at each allele are stochastic and highly dynamic, leading to frequent mosaicism.

126

127　**Downsizing of sgRNA-Cas9 activity by sgRNA modification**

128　　　　Consistent with our findings, to generate heterozygous genotypes, other

129　methods such as CORRECT have basically employed bi-allelic editing but introduced

130　some technical approaches, such as the use of mixed HDR templates, to control editing

131　outcomes of two alleles for heterozygosity[8,9,22]. We alternatively attempt to maximize

132　mono-allelic genome editing by reducing excessive activity of conventional sgRNA-Cas9.

133　Reducing amounts of the all-in-one plasmid or sgRNA-expressing plasmid failed to

134　increase the clones with mono-allelic indels (Fig. 2a and Extended Data Fig. 2). Next,

135　addition of 15-base stretches of guanine [15G], cytosine [15C], adenine [15A], and

136　thymidine [15T] to the 5' end of spacer sites was tested on the basis of previous reports

137　describing that a few additional guanines at the 5' end may potentially interrupt the sgRNA-

138　Cas9 activity[23,24] (Fig. 2b). Importantly, among them, [15C] extension substantially

139　increased frequency of mono-allelic indel clones (Fig. 2c). The [15T]sgRNA almost

140　completely failed to induce indel, which might be due to loss of sgRNA expression because

141　[15T] contained a 4xT transcription termination signal for the U6 promoter[25]. Thus, we

142　focused on cytosine ([C]) extension in the subsequent experiments.

143   We further investigated the relationships between [C] extension length and bi-

144   /mono-allelic indel patterns by systematically generating all-in-one-plasmids expressing

145   [0C]-[30C]-extended sgRNAs for six different sgRNA sequences (Fig. 2d and Extended

146   Data. Fig. 3, 4). For all six sgRNAs, [C]-extended sgRNAs ([C]sgRNAs) exhibited

147   decreased bi-allelic indels and increased mono-allelic indels in a length-dependent manner,

148   indicating length-dependent editing suppression (Fig. 2d). Allelic bias was not observed in

149   the case of mono-allelic indel induction (Fig. 2e and Extended Data Fig. 5a). Editing

150   efficiency is reportedly influenced by the local genome environment and cell types, even

151   when targeting the same sequences, as confirmed in Extended Data Fig. 5b, c, and highly

152   depends on the target sequences. In fact, the absolute indel probabilities of [C]sgRNAs

153   varied among several different sgRNAs (Fig. 2d and Extended Data Fig. 4a); nevertheless,

154   in all experiments, [C] extension exerted uniform suppression effects on diverse sgRNA

155   sequences. This effect can be explained by the assumption that [C] extension decreases the

156   effective sgRNA-Cas9 complex in a length-dependent manner, as supported by

157   computational modeling (Extended Data Fig. 4b, c and Methods). Accordingly, substantial

158   effect of [C] extension on DSB induction was also confirmed by an *in vitro* cleavage assay

159   using a fixed amount of [C]sgRNA (200 nM), Cas9 (66.7 nM), and template DNA (300

160   ng) (Fig. 2f). In addition, downsized sgRNA-Cas9 activity by [20C]sgRNAs increased the

161   frequency of mosaicism up to 63 %, while the frequency of mosaicism of conventional

162   system was approximately 30% (Fig. 2g, opened bars). These findings suggest that kinetics

163   of indel induction is delayed by [C] extension and that clonal analysis with dissociation

164   methods is critical for downstream applications, especially when downsized sgRNA-Cas9

165   is used.

166   We further investigated whether [C] extension allows both mono-allelic

167   insertion (knock-in, KI) of large gene cassettes via HDR and protection of non-HDR allele

168   from indel induction, i.e. one-step generation of HDR/WT clones (Fig. 2h and Extended

169   Data Fig. 5d-f). Overall HDR frequency, which included HDR/indel clones, gradually

170   decreased along with [C] extension due to the reduction in indel probability (Fig. 2h,

171   middle panels). Although the overall HDR frequency of [30C]sgRNA was 3-fold less than

172   that of [0C]sgRNA, the scarless HDR/WT frequency of [30C]sgRNA was 25-fold higher

173   than that of [0C]sgRNA (Fig. 2h, right panel). These data indicate that one scarless

174   HDR/WT clone can be theoretically obtained by picking 40 or 1.6 tdTomato-positive KI

175   clones when using [0C] or [30C]sgRNA, respectively. Similar result was obtained in AIMS

176   experiment, indicating that one scarless HDR/WT clone can be theoretically obtained by

177   picking 137 or 1.9 G418-resistant KI clones when using [0C] or [25C]sgRNA, respectively

178   (Extended Data Fig. 5d-f). Together, these findings suggest that mono-allelic HDR clones

179   without scar on another allele can be efficiently obtained by downsizing sgRNA-Cas9

180   activity.

181

182   **Computational modeling of single-cell heterogeneity of editing frequency**

183   In theory, maximum of the frequency of mono-allelic indel is 0.5 when setting

184   the indel probably to 0.5 if homogenous cell population was assumed. However, actual

185   frequency of mono-allelic indel (F(Mono)) was substantially lower than estimated

186   F(Mono) especially around the intermediate AIMS[P] levels (AIMS[P] ~ 0.5) (Fig. 3a, b).

187   Thus, we considered heterogeneity in genome editing frequency at the single-cell level and

188   computationally modeled the relationships between [C] extension and mono-allelic indel

9

189   based on AIMS datasets. By utilizing beta distribution and identifying the optimal setting

190   (α value of 0.715) (Extended Data Fig. 6a-d and Methods), we successfully predicted the

191   frequencies for bi-, mono-, and no-indel that highly matched to the AIMS data (Fig. 3b, c

192   and Extended Data Table 1). The simulation indicated that the highest frequency of mono-

193   allelic indel induction is 30.8% when AIMS[P] is 0.392 (Fig. 3d and Extended Data Table

194   2). In our experiments, [C] extension between 15 and 30 nucleotides is generally optimal

195   for mono-allelic indel induction (Fig. 2d and Extended Data. Fig. 4). Using this model, we

196   confirmed that both Bac[P] and AIMS[P] yields comparable predictions (Fig.3e) and

197   further observed that Bac[P]-based predictions could be applied even when targeting the

198   endogenous *Alb* gene (Fig. 3f). These results collectively suggest that heterogeneity in

199   editing efficiency is another obstacle for efficient mono-allelic editing and that continuous

200   fine-tuning of Cas9 activity is important to find the optimal range of Cas9 activity.

201   Next, we examined whether the frequency of compound heterozygous

202   mutation could be predicted using a Cdh1-P2A$_1$-AIMS (Fig. 3g). Compound heterozygous

203   clones were obtained only with the [25C]sgRNA combination, and the frequency of 0.50

204   (18 / 363) was almost identical to the predicted frequency of 0.36 (Fig. 3g), supporting high

205   accuracy of the prediction.

206

Generation of a heterozygous SNP disease model

208   Scarless mono-allelic single nucleotide editing is the most challenging

209   recombination because it involves a high probability of off-target cleavage against a 1 bp

210   mismatched (1mm) HDR allele[9]. We adopted [C] extension method to this issue. To

211   achieve this goal, we chose Fibrodysplasia Ossificans Progressiva (FOP) for which a

212   mono-allelic 617G > A (R206H) mutation in human *ACVR1* gene is a causal mutation[26]

213   and attempted to generate the identical mutation of mouse *Acvr1* gene in wild-type

214   (WT/WT) mESCs (Fig. 4a). A sgRNA was designed for the region crossing the G>A

215   editing site (Fig. 4a), and indel probability reduction by [C] extension was confirmed by

216   T7E1 and Bac[P] analysis (Fig. 4b, c). After transfection with all-in-one CRISPR plasmids

217   and ssODN as an HDR repair template, sequence analysis was performed for individual

218   clones and the frequencies of overall HDR and precise mono-allelic HDR (WT/R206H)

219   were determined. The overall HDR consists of WT/R206H genotype and all other

220   genotypes harboring indels. [0C]sgRNA induced overall HDR only in 4.1% of clones,

221   however, the frequency of overall HDR for [5C]sgRNA went up to 20.5% and the

222   frequency gradually decreased in parallel with the reduction in indel probability (Fig. 4d).

223   In contrast, the frequency of precise WT/R206H HDR gradually increased with [C]

224   extension, and all clones for [25C] and [30C]sgRNAs exhibited the correct WT/R206H

225   genotype, while [0C]-[10C]sgRNAs could not induce the precise editing (Fig. 4d). Based

226   on overall HDR frequency, we computationally estimated HDR rates after DNA cleavage

227   of single allele by taking into account heterogeneity of single-cell editing efficiency (Fig.

228   4e). This analysis clearly showed that low HDR rate (2.07 %) increases upon [C] extension

229   and that each [C]sgRNA exhibits similarly high HDR rate (mean 10.99%) except for [25C].

230   This suggests that [C] extension has generally recovered HDR rate presumably suppressed

231   by conventional CRISPR-Cas9 system.

232

233   **Suppression of off-target activity by CRISPR-Cas9 downsizing**

11

234   In spite of general increase in HDR rates, the precise WT/R206H clones were

235   obtained only for long [C] extension ([20C]-[30C]) but not for short [C] extension with

236   high overall HDR frequency. We assumed that suppressing Cas9 activity makes 1-

237   nucleotide mismatch (1mm) targets less responsive to off-target cleavage, thereby

238   protecting HDR allele from second indel induction. As shown in Fig. 4c, the ratio of off-

239   target editing on R206H HDR allele (1mm) to on-target editing on perfect matched (pf)

240   WT allele decreased along with [C] extension. Since differences in editing efficiency for

241   on-targets and off-targets reflects differences in their dissociation constants, in theory, the

242   ratio of off-target editing to on-target editing and on-target specificity decrease and increase

243   along with suppression of editing frequency, respectively (Extended Data Figure 7a, b and

244   Methods). Thus, protection of HDR allele from second editing becomes remarkable upon

245   long [C] extension. Consistently, the strong off-target inhibitory effect by [C] extension

246   was also confirmed for other sgRNAs in HEK293T cells (Extended Data Fig. 7c, d). We

247   further performed detailed computational modeling of various HDR outcomes based on

248   estimated HDR rates shown in Fig. 4e (Fig. 4f-g, Extended Data Fig. 8a-f, and Methods).

249   The predicted frequencies of overall HDR, WT/R206H HDR, and various HDR patterns

250   were highly consistent with the experimental results (Fig. 4f-h). The optimal indel

251   probability for the precise WT/R206H HDR was predicted to be 0.313, which was slightly

252   lower than the optimal indel probability of 0.392 for mono-allelic indel induction,

253   suggesting the use of [20C]sgRNA and [25C]sgRNA (Extended Data Fig. 8c).

254   Finally, we confirmed acquisition of the FOP phenotype in the WT/R206H

255   clone by generating chimeric mice. Ectopic ossification at their contributing sites was

256   confirmed (Fig. 4i), as reported in the previous work[27].

257

Safe and systematic precise gene correction in FOP hiPSCs

259   We next demonstrated the R206H allele-specific gene correction by

260   downsizing sgRNA-Cas9 activity in a FOP patient-derived human induced pluripotent

261   stem cells (hiPSCs, WT/ R206H)[28] (Fig. 5a). The sgRNA was designed for the R206H (pf)

262   allele and transfected with ssODN containing a silent mutation as a hallmark, which is

263   necessary to distinguish an HDR-corrected (Corrected) allele from original WT allele.

264   Otherwise, WT/- clones, in which PCR amplicons from R206H allele cannot to be obtained

265   due to large deletions or more complex genomic rearrangement[7], are misidentified as

266   WT/Corrected ones. Efficient indel induction by [0C]sgRNA and its decrease by [5C]-

267   [20C]sgRNAs were confirmed by a T7E1 assay (Fig. 5b). Bac[P] analysis showed that

268   indel probabilities on the WT (1mm) allele decreased with [5C]sgRNA more potently than

269   those on the R206H (pf) allele (Fig. 5c). As described above, the relative suppression of

270   off-target effects is explained by the inherent effects of suppressing on-target activities

271   (Extended Data Fig. 7). Corrected allele (2mm) is further less sensitive to second editing.

272   It is known that Cas9-mediated DSBs induce potent p53-dependent

273   cytotoxicity in hiPSCs[5,6]. Indeed, severe cytotoxicity was induced by [0C]sgRNA (Fig. 5d)

274   and p53 was highly activated in 86% of the surviving cells (Fig. 5e). In contrast, such

275   cytotoxicity and p53 activation were dramatically relieved by the use of [5C]-

276   [20C]sgRNAs (Fig. 5d, e). Inhibition of cytotoxicity by [C] extension was also confirmed

277   by independent experiments targeting other genes in hiPSCs (Extended Data Fig. 9a-d),

278   although HEK293T cells were tolerable to conventional system (Extended Data Fig. 9e-h).

279   We next determined the frequencies of overall HDR and precise WT/Corrected HDR.

13

280   Overall HDR frequency with [5C]sgRNA was comparable to that of [0C]sgRNA albeit

281   with a lower indel probability, and overall HDR frequency decreased with longer [C]

282   extension (Fig. 5f). The precise WT/Corrected clones could be obtained by [5C]sgRNA

283   and [10C]sgRNA, but not by [0C]sgRNA (Fig. 5f). As the result of gene correction, activin

284   A-mediated activation of bone morphogenetic protein (BMP)-responsive Smad1/5/8 was

285   cancelled in the WT/Corrected clone (Fig. 5g), as reported in the previous work[29].

286   We performed similar computational modeling of editing outcomes (Extended

287   Data Fig. 8a, 10a-e). The HDR rates of a single allele for [0C]sgRNA and [5C]-

288   [15C]sgRNAs were estimated to be 13.21% and 26.93%, respectively (Fig. 5h). The

289   predicted overall and WT/R206H HDR frequencies highly correlated with the

290   experimental results (Fig. 5i and Extended Data Fig. 10c). The computational model

291   estimated the frequency of all 12 possible HDR patterns, which suggested that two

292   populations   of   'WT_Corrected_indel/R206H_indel'   (fraction   12)   and

293   'WT_indel/R206H_Corrected_indel' (fraction 6) were dominant when indel probability

294   was high (Extended Data Fig. 10e, upper panels), suggesting that lowering indel probability

295   is necessary to prevent second editing and allow single-step precise editing. The optimal

296   indel probability for the precise HDR was simulated to be 0.424, suggesting the use of

297   [5C]sgRNA (Extended Data Fig. 10b, e).

298   Similar to the mESC data, HDR rate of [0C]sgRNA was estimated to be lower

299   than that of [5-15C]sgRNAs (Fig. 5h). Additional HDR experiment for 3 bp replacement

300   in HEK293T cells also showed HDR enhancement with [5C]sgRNA even though indel

301   probability was similar between [0C] and [5C]sgRNAs (Extended Data Fig. 10f-h). Here

302   we conclude that the precise heterozygous HDR clones can be systematically obtained by

14

303   downsizing sgRNA-Cas9 activity through multiple mechanisms, including enhancing

304   mono-allelic editing, suppressing p53-dependent cytotoxicity, increasing HDR rates, and

305   suppressing second cleavage of HDR-allele through off-target suppression (Fig. 5j).

306

307   **Discussion**

308   Various approaches, such as anti-Cas9 protein and small molecule inhibitor, have been

309   demonstrated to downsize Cas9 activity[14,30-36]. However, their significance in precise

310   genome editing and safety has not been well tested. Here we have established that simple

311   modifications of sgRNAs sufficiently enable fine-tuning of sgRNA-Cas9 activity, which

312   avoid the use of other molecules with unknown adverse effects.

313   Mono-allelic genome editing using the reduced activity of sgRNA-Cas9 is

314   important not only for generating heterozygous mutants and precise gene correction, but

315   also for protecting the genome from unwanted off-target mutations and cytotoxicity (Fig.

316   5j). Notably, we clarified an inhibitory effect of [C] extension on the off-target activity on

317   1mm targets and an enhancement of on-target specificity, although these 1 mm off-targets

318   had the same maximum indel probability as on-targets in the conventional system.

319   Conventional methods inevitably involve multistep editing to generate precise

320   heterozygous clones because HDR-allele have to be protected from second off-target

321   editing by introduction of silent mutations and the silent mutations should be re-corrected

322   especially for non-coding regions[9]. On the other hand, [C] extension methods enable single

323   step heterozygous editing by protecting HDR-allele through direct suppression of off-target

324   effects. This would be beneficial for convenient modeling of heterozygous states of disease

325   mutations and risk variants and investigation of their downstream effects such as allele-

326   specific epigenome and gene regulation. In our system, precise homozygous mutations can

327   be obtained by repeated mono-allelic editing. Our finding is consistent with the context of

328   previous studies suggesting that the increased on-target specificity of engineered Cas9s,

329   truncated gRNAs, and gRNAs with a couple of guanine addition to the 5' end, is at least

330   partially due to decrease in the activity of sgRNA-Cas9 complex[24,37,38].

331   Another important hallmark of [C] extension is suppression of excess DNA

332   damage and cytotoxicity, leading to enhancement of HDR. The previous work reported

333   that p53 activation induces cytotoxicity and inhibits HDR frequency by 19-fold in hiPSCs[6].

334   We conspicuously demonstrated that even short [C] extension such as [5C]sgRNA had

335   strong potential to reduce p53 activation, enhance cell viability, and HDR rates, while

336   maintaining maximum on-target activity. Thus, to avoid any long-term deleterious effects

337   of excessive DNA damage on cell phenotypes, it may be reasonable to consider the use of

338   sgRNAs with short [C] extension, such as [5C]sgRNA, as the next-generation CRISPR-

339   Cas9 platform for diverse applications in mammalian cells. Furthermore, tunable

340   downsizing of Cas9 activity, presented in this study, offers a systematic and safeguard

341   platform for switchable use of bi-allelic and mono-allelic genome editing.

342

Main References

343
344

345   1   Jinek, M. *et al.* A programmable dual-RNA-guided DNA endonuclease in adaptive
346   bacterial immunity. *Science* **337**, 816-821, doi:10.1126/science.1225829 (2012).
347   2   Cong, L. *et al.* Multiplex genome engineering using CRISPR/Cas systems. *Science*
348   **339**, 819-823, doi:10.1126/science.1231143 (2013).
349   3   Mali, P. *et al.* RNA-guided human genome engineering via Cas9. *Science* **339**, 823-
350   826, doi:10.1126/science.1232033 (2013).
351   4   Cho, S. W., Kim, S., Kim, J. M. & Kim, J. S. Targeted genome engineering in
352   human cells with the Cas9 RNA-guided endonuclease. *Nat Biotechnol* **31**, 230-232,
353   doi:10.1038/nbt.2507 (2013).
354   5   Haapaniemi, E., Botla, S., Persson, J., Schmierer, B. & Taipale, J. CRISPR-Cas9
355   genome editing induces a p53-mediated DNA damage response. *Nat Med* **24**, 927-
356   930, doi:10.1038/s41591-018-0049-z (2018).
357   6   Ihry, R. J. *et al.* p53 inhibits CRISPR-Cas9 engineering in human pluripotent stem
358   cells. *Nat Med* **24**, 939-946, doi:10.1038/s41591-018-0050-6 (2018).
359   7   Kosicki, M., Tomberg, K. & Bradley, A. Repair of double-strand breaks induced
360   by CRISPR-Cas9 leads to large deletions and complex rearrangements. *Nat*
361   *Biotechnol* **36**, 765-771, doi:10.1038/nbt.4192 (2018).
362   8   Soldner, F. *et al.* Parkinson-associated risk variant in distal enhancer of alpha-
363   synuclein   modulates   target   gene   expression.   *Nature*   **533**,   95-99,
364   doi:10.1038/nature17939 (2016).
365   9   Paquet, D. *et al.* Efficient introduction of specific homozygous and heterozygous
366   mutations using CRISPR/Cas9. *Nature* **533**, 125-129, doi:10.1038/nature17664
367   (2016).
368   10 Komor, A. C., Kim, Y. B., Packer, M. S., Zuris, J. A. & Liu, D. R. Programmable
369   editing of a target base in genomic DNA without double-stranded DNA cleavage.
370   *Nature* **533**, 420-424, doi:10.1038/nature17946 (2016).
371   11 Nishida, K. *et al.* Targeted nucleotide editing using hybrid prokaryotic and
372   vertebrate adaptive immune systems. *Science* **353**, doi:10.1126/science.aaf8729
373   (2016).
374   12 Gaudelli, N. M. *et al.* Programmable base editing of A*T to G*C in genomic DNA
375   without DNA cleavage. *Nature* **551**, 464-471, doi:10.1038/nature24644 (2017).
376   13 Anzalone, A. V. *et al.* Search-and-replace genome editing without double-strand
377   breaks or donor DNA. *Nature* **576**, 149-157, doi:10.1038/s41586-019-1711-4
378   (2019).
379   14 Lee, H. K. *et al.* Targeting fidelity of adenine and cytosine base editors in mouse
380   embryos. *Nat Commun* **9**, 4804, doi:10.1038/s41467-018-07322-7 (2018).
381   15 Kim, H. S., Jeong, Y. K., Hur, J. K., Kim, J. S. & Bae, S. Adenine base editors
382   catalyze cytosine conversions in human cells. *Nat Biotechnol* **37**, 1145-1148,
383   doi:10.1038/s41587-019-0254-4 (2019).
384   16 Lin, Q. *et al.* Prime genome editing in rice and wheat. *Nat Biotechnol* **38**, 582-585,
385   doi:10.1038/s41587-020-0455-x (2020).

386   17   Liu, Y. *et al.* Efficient generation of mouse models with the prime editing system.
387   *Cell Discov* **6**, 27, doi:10.1038/s41421-020-0165-z (2020).
388   18   Kim, J. H. *et al.* High cleavage efficiency of a 2A peptide derived from porcine
389   teschovirus-1 in human cell lines, zebrafish and mice. *PLoS One* **6**, e18556,
390   doi:10.1371/journal.pone.0018556 (2011).
391   19   Russell, R. *et al.* A Dynamic Role of TBX3 in the Pluripotency Circuitry. *Stem Cell*
392   *Reports* **5**, 1155-1170, doi:10.1016/j.stemcr.2015.11.003 (2015).
393   20   Pieters, T. *et al.* p120 Catenin-Mediated Stabilization of E-Cadherin Is Essential
394   for Primitive Endoderm Specification. *PLoS Genet* **12**, e1006243,
395   doi:10.1371/journal.pgen.1006243 (2016).
396   21   Chari, R., Mali, P., Moosburner, M. & Church, G. M. Unraveling CRISPR-Cas9
397   genome engineering parameters via a library-on-library approach. *Nat Methods* **12**,
398   823-826, doi:10.1038/nmeth.3473 (2015).
399   22   Maurissen, T. L. & Woltjen, K. Synergistic gene editing in human iPS cells via cell
400   cycle and DNA repair modulation. *Nat Commun* **11**, 2876, doi:10.1038/s41467-
401   020-16643-5 (2020).
402   23   Cho, S. W. *et al.* Analysis of off-target effects of CRISPR/Cas-derived RNA-
403   guided endonucleases and nickases. *Genome Res* **24**, 132-141,
404   doi:10.1101/gr.162339.113 (2014).
405   24   Mullally, G. *et al.* 5' modifications to CRISPR-Cas9 gRNA can change the
406   dynamics and size of R-loops and inhibit DNA cleavage. *Nucleic Acids Res* **48**,
407   6811-6823, doi:10.1093/nar/gkaa477 (2020).
408   25   Arimbasseri, A. G., Rijal, K. & Maraia, R. J. Transcription termination by the
409   eukaryotic RNA polymerase III. *Biochim Biophys Acta* **1829**, 318-330,
410   doi:10.1016/j.bbagrm.2012.10.006 (2013).
411   26   Shore, E. M. *et al.* A recurrent mutation in the BMP type I receptor ACVR1 causes
412   inherited and sporadic fibrodysplasia ossificans progressiva. *Nat Genet* **38**, 525-
413   527, doi:10.1038/ng1783 (2006).
414   27   Chakkalakal, S. A. *et al.* An Acvr1 R206H knock-in mouse has fibrodysplasia
415   ossificans progressiva. *J Bone Miner Res* **27**, 1746-1756, doi:10.1002/jbmr.1637
416   (2012).
417   28   Matsumoto, Y. *et al.* Induced pluripotent stem cells from patients with human
418   fibrodysplasia ossificans progressiva show increased mineralization and cartilage
419   formation. *Orphanet J Rare Dis* **8**, 190, doi:10.1186/1750-1172-8-190 (2013).
420   29   Hino, K. *et al.* Neofunction of ACVR1 in fibrodysplasia ossificans progressiva.
421   *Proc Natl Acad Sci U S A* **112**, 15438-15443, doi:10.1073/pnas.1510540112
422   (2015).
423   30   Pawluk, A. *et al.* Naturally Occurring Off-Switches for CRISPR-Cas9. *Cell* **167**,
424   1829-1838 e1829, doi:10.1016/j.cell.2016.11.017 (2016).
425   31   Harrington, L. B. *et al.* A Broad-Spectrum Inhibitor of CRISPR-Cas9. *Cell* **170**,
426   1224-1233 e1215, doi:10.1016/j.cell.2017.07.037 (2017).
427   32   Rauch, B. J. *et al.* Inhibition of CRISPR-Cas9 with Bacteriophage Proteins. *Cell*
428   **168**, 150-158 e110, doi:10.1016/j.cell.2016.12.009 (2017).
429   33   Bubeck, F. *et al.* Engineered anti-CRISPR proteins for optogenetic control of
430   CRISPR-Cas9. *Nat Methods* **15**, 924-927, doi:10.1038/s41592-018-0178-9 (2018).

431 34 Hynes, A. P. *et al.* Widespread anti-CRISPR proteins in virulent bacteriophages
432   inhibit a range of Cas9 proteins. *Nat Commun* **9**, 2919, doi:10.1038/s41467-018-
433   05092-w (2018).
434 35 Jiang, F. *et al.* Temperature-Responsive Competitive Inhibition of CRISPR-Cas9.
435   *Mol Cell* **73**, 601-610 e605, doi:10.1016/j.molcel.2018.11.016 (2019).
436 36 Maji, B. *et al.* A High-Throughput Platform to Identify Small-Molecule Inhibitors
437   of CRISPR-Cas9. *Cell* **177**, 1067-1079 e1019, doi:10.1016/j.cell.2019.04.009
438   (2019).
439 37 Singh, D. *et al.* Mechanisms of improved specificity of engineered Cas9s revealed
440   by single-molecule FRET analysis. *Nat Struct Mol Biol* **25**, 347-354,
441   doi:10.1038/s41594-018-0051-7 (2018).
442 38 Okafor, I. C. *et al.* Single molecule analysis of effects of non-canonical guide RNAs
443   and specificity-enhancing mutations on Cas9-induced DNA unwinding. *Nucleic*
444   *Acids Res* **47**, 11880-11888, doi:10.1093/nar/gkz1058 (2019).
445

446 **Methods**

447

448 **Cell culture**

449 mESCs were cultured in t2iL medium containing DMEM (Nacalai Tesque) with 2 mM

450 Glutamax (Nacalai Tesque), $1 \times$ non-essential amino acids (NEAA) (Nacalai Tesque), 1

451 mM Sodium Pyruvate (Nacalai Tesque), 100 U/ml penicillin, 100 μg/ml streptomycin (P/S)

452 (Nacalai Tesque), 0.1 mM 2-mercaptoethanol (SIGMA) and 15% fetal bovine serum (FBS)

453 (GIBCO), supplemented with 0.2 μM PD0325901 (SIGMA), 3 μM CHIR99021 (Cayman)

454 and 1,000 U/ml recombinant mouse LIF (Millipore)[39]. Higher concentration of PD0325901

455 at 1 μM was also used for 2iL medium. mESC colonies were dissociated with trypsin

456 (Nacalai Tesque) and plated on gelatin-coated dishes. Y-27632 (10 μM, SIGMA) was

457 added when cells were passed. hiPSCs were cultured in mTeSR Plus medium (VERITAS).

458 hiPSC colonies were dissociated with Accutase (Nacalai Tesque) and plated on matrigel-

459 coated dishes (matrigel, CORNING, 3/250 dilution with DMEM). Y-27632 and 1% FBS

460 were added when cells were passed. WT hiPSCs (409B2, HPS0076) were provided by the

461 RIKEN BRC[40]. FOP hiPSCs (HPS0376) were provided by the RIKEN BRC through the

462 National BioResource Project of the MEXT/AMED, Japan[28]. The study using hiPSCs was

463 approved by the Kyushu University Institutional Review Board for Human Genome/Gene

464 Research. HEK293T cells and mouse embryonic fibroblasts (MEFs) were cultured in 10%

465 FBS medium containing DMEM, 2 mM l-glutamine (Nacalai Tesque), 100 U/ml penicillin,

466 100 μg/ml streptomycin (P/S) (Nacalai Tesque) and 10% FBS. Cells were maintained at

467 37 °C with 5% CO_2.

468

469 **Animals**

470 C57BL/6 mice (Clea Japan, Tokyo, Japan), ICR mice (Clea Japan, Tokyo, Japan) and

471 $R26R^{YFP/YFP}$ mice[41] (a gift from Frank Costantini, Columbia University, New York, NY)

472 were used in the present study. The experiments were approved by the Kyushu University

473 Animal Experiment Committee, and the care and use of the animals were performed in

474 accordance with institutional guidelines.

475

476 **Oligo nucleotides**

477 All primers, spacer linkers, and ssODNs used in the present study are listed in the Extended

478 Data Table 3.

479

480 **Establishing mESCs**

481 Mouse ES cell lines of B6-5-2 and B6-D2-4 line were established from E3.5 blastocysts of

482 C57BL/6 strain using 2iL or t2iLmedium, respectively, and a mESC line of $R26R^{YFP/+}$

483 mouse strain was established using t2iL medium. Blastocysts were placed on feeders

484 (mitomycin C-treated MEFs) after removing zona pellucida. Outgrowths of the inner cell

485 mass (passage number 0, p0) were dissociated with trypsin and plated on gelatin-coated

486 plate (p1). After domed colonies were grown, they were dissociated and passed (p2). The

487 mESC lines were generated by repeating this procedure.

488

489 **Generation of AIMS**

490 Knock-in (KI) template plasmids for Cdh1-AIMS were generated by attaching 5' and 3'

491 arms to plasmids containing $P2A_1$:Venus or $P2A_1$:tdTomato cassettes. The $P2A_1$ is

21

492 identical to a P2A sequence which is generally used[18]. The 5' arm was designed so that the

493 coding end is fused to the P2A sequence in-frame to allow the production of both E-

494 cadherin (CDH1) and the fluorescence protein independently. The KI plasmids for Tbx3-

495 AIMS were constructed using the same strategy. The alternative P2A sequence P2A$_2$ was

496 constructed by introducing silent mutations to each codon of the original P2A sequence.

497 Conventional CRISPR-Cas9 system was used to efficiently knock-in the dual color

498 plasmids in a pair of alleles. A spacer linker was designed to induce DSB downstream of

499 the stop codon, and was inserted into *BpiI* sites of a pSpCas9(BB)-2A-Puro (PX459) V2.0

500 plasmid (Addgene, Plasmid #62988). All sgRNAs used in the present study were designed

501 using CRISPR DESIGN (http://crispr.mit.edu/) or CRISPOR (http://crispor.tefor.net).

502   Both the constructed all-in-one CRISPR plasmids and dual colored KI

503 plasmids were co-transfected into the mESCs using lipofectamine 3000 (Thermo Fisher

504 Scientific). Dissociated mESCs were plated on gelatin-coated 24-well plates with 500 μl

505 of (t)2iL+Y-27632 medium ((t)2iL+Y). Nucleic acid-Lipofectamine 3000 complexes were

506 prepared according to the standard Lipofectamine 3000 protocol. One μl of Lipofectamine

507 3000 reagent was added to 25 μl Opti-MEM medium, while 250 ng of each plasmid (all-

508 in-one, Cdh1-P2A-tdTomato, and Cdh1-P2A-Venus plasmid) plus 1 μl of P3000 reagent

509 were mixed with 25 μl of Opti-MEM medium in a different tube. These mixtures were

510 combined and incubated for 5 min at room temperature, and then added to the 24-well plate

511 just after cells were seeded. Twenty-four hours after transfection, puromycin (1.5 or 2

512 μg/ml) was added for 2 days, and then washed out. The transiently treated-puromycin

513 resistant cells were cultured for several days, and dual color-positive colonies were picked

514 and passed. The genotypes for candidate dual KI clones were confirmed by PCR.

515   Transfection experiments for mouse and human cells were performed according to this

516   procedure, and a couple of passage steps are added when AIMS assay was performed to

517   avoid mosaicism (Fig. 1d). Fluorescent microscopes (BZ-X800, KEYENCE and IX73,

518   OLYMPUS) were used to analyze the AIMS data.

519   To extract genomic DNA for the clonal sequence analysis, single mESC and

520   hiPSC colonies were suspended in 5-10 μl of 50 mM NaOH (Nacalai Tesque) and

521   incubated at 99 °C for 10 minutes.

522

523   **Plasmid construction**

524   To generate all-in-one CRISPR plasmids for [5C](3A), [10C](8A), [15C](13A),

525   [20C](18C), [25C](23A) and [30C](28A)sgRNA expression, spacer linkers were inserted

526   into the *BpiI* sites of a PX459 plasmid (Extended Data Fig. 3). In the plasmids, 3rd, 8th, 13th,

527   18th, 23rd or 28th cytosine was replaced with adenine since overhang sequence of CACC is

528   required for linker ligation. The standard spacer linkers were inserted into the *BpiI* sites of

529   the [5C](3A), [10C](8A), [15C](13A), [20C](18A), [25C](23A) or [30C](28A) PX459

530   plasmid, leading to generation of [5C]-[30C]sgRNA expressing all-in-one plasmids.

531   For a plasmid dilution assay, sgRNA expressing plasmid was constructed by

532   removing a Cas9-T2A-Puro cassette from a PX459 plasmid using *KpnI* and *NotI* sites. The

533   different amount of sgRNA expressing plasmid (0-250 ng) was co-transfected with

534   unmodified PX459 plasmid (250 ng).

535

536   *In vitro* **DNA cleavage assay**

537   For preparation of template DNA to be cleaved, 951 bp fragment was amplified by PCR

538   using a Tbx3-P2A$_1$-Venus KI plasmid. The [0C], [10C] and [25C]sgRNAs were

539   synthesized by *in vitro* transcription (IVT) using a T7 RiboMAX Express Large Scale RNA

540   Production System (Promega) according to the manufacture's protocol. The template DNA

541   fragments required for IVT were amplified by PCR using forward and reverse primers. The

542   T7 promoter sequence and cytosine tails were added to 5' end of the forward primer. Cas9

543   protein (IDT) was suspended with a Diluent B (NEB) to make 1 μM solution. The 10 ×

544   Cas9 reaction buffer contains 1 M HEPES, 3 M NaCl, 1 M MgCl$_2$, and 250 mM EDTA

545   (pH6.5). For cleavage, 1 μl of Cas9 (1 μM), 1μl of [C]sgRNAs (3 μM), 1 μl of 10 × Cas9

546   reaction buffer, and 3 μl of template DNA (100 ng/μl) were mixed with 9 μl of distilled

547   water (Total 15 μl reaction volume) and reacted at 37 °C for 1 hour.

548

549   **Scarless mono-allelic KI of tdTomato or P2A$_1$-Neo cassette**

550   A Tbx3-P2A$_1$-tdTomato KI plasmid was co-transfected with Tbx3-sgRNA1-expressing

551   PX459 to the mESCs. After transient puromycin selection, colonies were passed after

552   dissociation and the subsequent colonies were analyzed. The colonies with mosaic

553   tdTomato expression were excluded for the data analysis. After counting the colony

554   number, tdTomato positive colonies were picked and genomic DNA was extracted for

555   sequencing.

556   Neomycin (Neo) KI plasmid was constructed by replacing tdTomato cassette

557   of the Tbx3-P2A$_1$-tdTomato KI plasmid with a P2A$_1$-Neo cassette. The KI plasmid was

558   co-transfected with P2A$_1$ sgRNA1-expressing PX459 to a Tbx3-P2A$_1$-AIMS clone. When

559   puromycin was removed, geneticin (400 μg/ml, GIBCO) were added to select KI clones.

24

560 As analyzed all 8 clones were confirmed to have successful KI genotypes, geneticin-

561 resistant colonies were counted as KI.

562

563 **T7E1 assays**

564 PCR reactions to amplify specific on-target or off-target sites were performed using KOD-

565 Plus-ver.2 DNA polymerase (TOYOBO) according to the manufacture's protocol.

566 Resulting PCR amplicons were denatured and re-annealed in $1 \times$ NEB buffer 2 (NEB) in a

567 total volume of 9 µl using a following conditions: 95 °C for 5 min; 95 °C to 25 °C ramping

568 at -0.1 °C /s, and hold at 4 °C. After re-annealing, 1 µl of T7 Endonuclease I (NEB, 10

569 units/µl) was added and incubated at 37 °C for 15 min.

570

571 **Bac[P] assays**

572 Purified PCR products which amplified specific on-target or off-target sites were inserted

573 into a T-easy vector (Promega) and transformed into DH5-α bacterial cells. To enable rapid

574 and efficient indel detection, plasmids were directly isolated from each white colony (blue

575 white screening was done), and inserted DNA fragment was amplified by PCR. The PCR

576 amplicons were mixed with the PCR products which were amplified from wild-type DNA

577 template such as KI plasmids or unedited genomic DNA, and T7E1 assay was performed.

578 Sanger sequencing was also performed for the PCR amplicons, which were not digested

579 by T7E1, to determine the total number of colony harboring an indel. The Bac[P] value

580 was calculated by the following formula: Bac[P] = *Indel* /*Total*.

581 Bac[P] values for both WT and R206H alleles were determined with the

582 experiments inducing indels using various [C]sgRNAs in the mESC clone of the FOP

583   model. The targeting sites of both WT and R206H alleles were amplified by PCR and were

584   cloned into T-easy vector. Sanger sequencing was performed for each PCR product derived

585   from single bacterial clones as described above. Similarly, Bac[P] values for both R206H

586   (pf) and WT (1 mm) alleles were determined by inducing indels in the FOP hiPSCs, while

587   a corrected cell line (WT/Corrected) was used to determine Bac[P] value of the corrected

588   allele (2 mm). Since some PCR products do not contain a G/A hallmark due to

589   intermediate-sized deletions from 12 to about 50 nucleotides, it is not possible to determine

590   which allele was edited for these PCR products. We observed that the fraction of such

591   products with intermediate-sized deletions was relatively constant (approximately 20 % in

592   the experiments in Fig. 4 and 10~20 % in the experiments in Fig. 5) and did not decrease

593   along [C] extension, suggesting that the intermediate-sized deletions are byproducts of

594   short indel induction processes. We therefore assigned to the products with intermediate-

595   sized deletions to two alleles using the ratio of PCR products whose origins were

596   convincingly confirmed. For the analysis in Fig. 5, averages of Bac[P] for WT (1 mm)

597   allele based on comparisons of (1) R206H (pf) and WT (1 mm) alleles and (2) WT (1 mm)

598   and corrected (2 mm) alleles were used for the subsequent computational analysis.

599

600   **Cellular viability assays**

601   Based on the transfection protocol described above ('Generation of AIMS'), 2×10^5 WT

602   hiPSCs or 4×10^4 HEK293T cells were seeded on the 48-well plate and transfected with

603   100 ng of the all-in-one CRISPR plasmids (2/5 scale of 24-well plate version). The hiPSCs

604   cells were dissociated and counted using trypan blue 3 or 4 days after the transient

605   puromycin treatment at 1.5 μg/ml, while HEK293T cells were counted 4 days after the

606   transient puromycin treatment at 3 μg/ml.

607

608   **Generation and correction of a FOP model via HDR with ssODNs**

609   The transfection protocol for 24-well plate experiment is described above ('Generation of

610   AIMS'). For HDR induction in mESCs and HEK293T cells, 1 μl of 10 μM ssODN

611   (eurofins) was added to the plasmid-lipofectamine complex, whereas 1 μl of 3 μM ssODN

612   was added when hiPSCs were transfected since 10 μM concentration induced severe

613   toxicity. After transient puromycin selection, colonies were dissociated and plated at low

614   density to avoid mosaicism. Single colonies were picked and genomic DNA was extracted.

615   Sequence analysis was performed to identify G to A replacement with or without indel. For

616   the correction of the FOP hiPSCs, clones receiving HDR were screened by digesting PCR

617   product using *BstUI* restriction enzyme (NEB), and then the *BstUI*-positive PCR products

618   were sequenced.

619

620   **Immunocytochemical analysis**

621   For p53 staining, transfection for HDR induction was performed in 1/5 scale of a 24-well

622   plate experiment, according to the protocol described above. In this assay, 6×10^4 hiPSCs

623   were seeded on a matrigel-coated 96-well plate in triplicate. Puromycin selection was

624   performed to examine p53 activity only in the transfected cells. The survived cells were

625   fixed with 4% PFA two days after puromycin removal. For pSmad1/5/8 staining, 5×10^3

626   cells were plated on a matrigel-coated 96-well plate without Y-27632 and 1% FBS. After

627   2.5 h culture, Activin-A (100 ng/ml) (R&D Systems) was treated for 30 min, and the cells

27

628   were fixed with 4% PFA. Antibody reaction was performed following standard protocols.

629   Rabbit polyclonal p53 (FL-393, Santa Cruz, 1:200) and rabbit monoclonal pSmad1/5/8

630   (D5B10, Cell Signaling Technology, 1:1000) antibodies were reacted overnight at 4 °C. A

631   donkey anti-rabbit Alexa Fluor 488 secondary antibody (Thermo Scientific, 1:1000) was

632   reacted RT for 30 min. Data analysis was performed by a cell count application of a

633   fluorescent microscope to select cells with p53 and pSmad1/5/8 activation by setting

634   fluorescence intensity thresholds (BZ-X800, KEYENCE).

635

636   **Chimera generation**

637   A mESC clone of a FOP model (C57BL/6 strain) was dissociated with trypsin and 5-8 cells

638   were injected into the 8-cell embryos (E2.5) harvested from ICR pregnant mice. Injected

639   blastocysts were transferred into the uteri of pseudo-pregnant ICR mice. Chimeric

640   contribution was confirmed by coat-color and YFP fluorescence. YFP was observed using

641   a fluorescence stereo microscope (M165FC, Leica).

642

643   **Computational modeling and analysis of single-cell level genome editing, [C]**

644   **extension, and HDR efficiency.**

645

646   **Comparison of AIMS[P] and Bac[P]**

647   In our study, the probability of single allele editing (P) is determined by two ways: (1)

648   AIMS and (2) Bac[P] assay based on T7E1 assay and complementation by sequence

649   validation. AIMS-based P (AIMS[P]) was determined as:

650
$$AIMS[P] = \frac{\left(2F(Bi) + F(Mono)\right)}{2} \tag{1}$$

651   , where F(Bi) and F(Mono) are the experimental frequency of cells with bi-allelic and

652   mono-allelic genome editing.

653   In the initial phase of the study, we compared matched AIMS[P] and Bac[P]

654   for nine sgRNAs (Cdh1-P2A1-sgRNA1 with different lengths of [C] extension) and

655   observed that AIMS[P] correlated well with Bac[P] (Extended Data Fig. 6a). In the

656   subsequent analyses, we used AIMS[P] for modeling of indel insertion frequency in

657   Figures 2 and 3 and Bac[P] for modeling of HDR frequency in Figures 4 and 5.

658

659   **Modeling of genome editing frequency at the single-cell level**

660   We performed extensive analysis by combining AIMS and generation of sgRNAs with

661   various [C] extension. When the editing efficiency is homogenous across the cell

662   population, the frequency of cells with bi-allelic, mono-allelic or no genome editing, F(Bi),

663   F(Mono), or F(No) can be estimated as:

664    $$F(Bi) = AIMS[P]^2 \tag{2}$$

665    $$F(Mono) = 2AIMS[P](1 - AIMS[P]) \tag{3}$$

666    $$F(No) = (1 - AIMS[P])^2 \tag{4}$$

667   We first used these equations and observed that actual F(Mono) is lower than estimated

668   F(Mono) especially around the intermediate AIMS[P] levels (AIMS[P] ~ 0.5). Thus,

669   heterogeneity in genome editing frequency at the single-cell level was considered and

670   modeled using beta distribution. Probability density

671   functions of P and mean P (E(P)) are given by:

672    $$f(P; \alpha, \beta) = \frac{P^{\alpha-1}(1 - P)^{\beta-1}}{B(\alpha, \beta)} \tag{5}$$

$$E(P) = \frac{\alpha}{\alpha + \beta} \qquad (6)$$

673

674 Mean P corresponds to AIMS[P] (or Bac[P]). Using beta distribution, F(Bi), F(Mono),

675 F(No) can be described as:

$$F(Bi) = \int_0^1 P^2 f(P; \alpha, \beta) dP \qquad (7)$$

676

$$F(Mono) = \int_0^1 2P(1 - P)f(P; \alpha, \beta) dP \qquad (8)$$

677

$$F(No) = \int_0^1 (1 - P)^2 f(P; \alpha, \beta) dP \qquad (9)$$

678

679   Using these equations, we first determined α value for each experiment that

680 minimized squared residuals between experimental F(Bi), F(Mono), and F(No) and

681 simulated F(Bi), F(Mono), and F(No) (Extended Data Fig. 6b). As shown in Extended Data

682 Fig. 6b, we observed that optimized α values were relatively constant in a wide range of

683 AIMS[P] (0.1 < AIMS[P] < 0.9). Thus, we next used the sum of squared residuals (SSR)

684 as the error function: SSR = $\sum$(Experimental data − Simulated data)^2, and determined a

685 constant α value that minimized SSR (Extended Data Fig. 6c, left, $\alpha = 0.715$). Probability

686 density functions with different mean P are shown in a middle panel of Extended Data Fig.

687 6c. We confirmed that introduction of beta distribution greatly reduced SSR compared to

688 the setting of homogenous editing frequency (Extended Data Fig. 6c, right) and well

689 explained the experimental F(Bi), F(Mono), and F(No) along diverse AIMS[P] (Extended

690 Data Fig. 6d). In addition, we tested normal distribution to approximate the heterogeneity

691 in genome editing frequency at the single-cell level, but observed that beta distribution was

692 superior to normal distribution.

693

694 **Effects of [C] extension on CRISPR-Cas9 system**

695 The efficiency of the single-allele editing P (P(pf); pf: perfect match) can be described as:

696
$$P(pf) = \frac{S}{K + S} \tag{10}$$

697 , where the concentration of effective sgRNA-Cas9 complexes and the dissociation

698 constant between the sgRNA and its target site are defined as S and K, respectively. Based

699 on high editing efficiency without [C] extension (P ~ 1), we assumed that the recovery rate

700 from single-site damage is very low and did not consider in subsequent analysis. To

701 mechanistically understand the effects of [C] extension and 1 mismatch, we further

702 assumed that [C] extension and 1mismatch decreases S and increases K, respectively. By

703 setting S to 1 for each of different sgRNA sequences without [C] extension, we first

704 approximated K values for each of different sgRNA sequences (8 sgRNA sequences).

705 When P (AIMS[P] or Bac[P]) was 1, P was set to 0.99. Next, relative S concentrations were

706 determined using K and AIMS[P] for sgRNAs with [C] extension. While the relationships

707 between [C] extension and AIMS[P] varied among different sgRNA sequences (Extended

708 Data Fig. 4a), we found clear and similar inverse relationships between [C] extension and

709 relative S values for different sgRNA sequences (Extended Data Fig. 4b). A linear

710 regression gave a good fit to logarithm of relative S against the length of [C] extension for

711 all sgRNA sequences (Extended Data Fig. 4b). Furthermore, analysis of covariance

712 (ANCOVA) indicated that slopes of linear regression did not significantly differ among

713 various sgRNA sequences (Extended Data Fig. 4c). This suggests that [C] extension exerts

714 uniform suppression effects on diverse sgRNA sequences.

715

716 **Effect of cytosine extension on specificity of CRISPR-Cas9 system**

717   As described above, 1mm (or 2mm) is considered to increase K in the equation (10). The

718   efficiency of the single-gene editing P on 1mm (or 2mm) target can be described as:

719
$$P(1mm \ or \ 2mm) = \frac{S}{mK + S} \qquad (11)$$

720   , where m is the ratio of K for 1mm target to K for perfect match target.

721   Thus, the single-gene editing P on 1mm (or 2mm) can be expressed as the function of P(pf)

722   as:

723
$$P(1mm \ or \ 2mm) = \frac{P(pf)}{(1 - m)P(pf) + m} \qquad (12)$$

724   For the results in Figures 4 and 5, we determined m that fits to matched P(pf) and P(1mm

725   or 2mm) by using SSR as the error function (Extended Data Fig. 7a).

726   The ratios between P(pf) vs. P(1mm or 2mm) are also described as the function of P(pf)

727   as:

728
$$\frac{P(1mm \ or \ 2mm)}{P(pf)} = \frac{1}{(1 - m)P(pf) + m} \qquad (13)$$

729
$$\frac{P(pf)}{P(1mm \ or \ 2mm)} = (1 - m)P(pf) + m \qquad (14)$$

730   As shown in Extended Data Fig. 7b, decreasing P(pf) contributes to reduction of relative

731   off-target ratio and increases in specificity. Thus, downsizing CRISPR-Cas9 activities by

732   [C] extension is also beneficial for reduction of relative off-target activities and

733   enhancement in specificity.

734

735   **Modeling of HDR frequency from homozygous states (Figure 4)**

736   Using beta distribution, frequencies of the various HDR clones in Figure 4 are determined

737   as follows (Extended Data Fig. 8a, b):

738
$$F(WT/R206H) = \int_0^1 2hP(1-P)(1-(1-h)P')f(P;\alpha,\beta)dP \qquad (15)$$

739
$$F(WT/R206H + indel) = \int_0^1 2h(1-h)P(1-P)P'f(P;\alpha,\beta)dP \qquad (16)$$

740
$$F(indel/R206H) = \int_0^1 2h(1-h)P^2(1-(1-h)P')f(P;\alpha,\beta)dP \qquad (17)$$

741
$$F(indel/R206H + indel) = \int_0^1 2h(1-h)^2P^2P'f(P;\alpha,\beta)dP \qquad (18)$$

742
$$F(R206H/R206H) = \int_0^1 h^2P^2f(P;\alpha,\beta)dP \qquad (19)$$

743
$$F(overall\ HDR) = \int_0^1 (-h^2P^2 + 2hP)f(P;\alpha,\beta)dP \qquad (20)$$

744 , where efficiency of HDR on Cas9-cleaved single allele and the probability of the single-

745 gene editing on edited target, i.e. 1mm target, are defined as h and P´, respectively

746 (Extended Data Fig. 8b). P´ is described in the same manner to equation (12):

747
$$P' = \frac{P}{(1-m)P+m} \qquad (21)$$

748 , where m is 1.723. [C] extension decreases P according to the length of [C] extension

749 (Extended Data. Fig. 8c).

750 For simplicity, h was considered to be constant across cell population for each

751 experiment. Based on the experimental results of overall HDR frequencies and the equation

752 (eq. #20), h was estimated for each [C] extended sgRNA (Fig. 4e). While h without [C]

753 extension was very low (2.07%), h with [C] extension was generally high around 11%.

754 This suggests that conventional system without [C] extension reduces HDR and [C]

755 extension releases the suppression to the upper limit of HDR. Based on these findings, we

756 used mean of estimated h (10.99%) as the h for [C] extended sgRNAs and estimated the

33

757   frequency of distinct HDR patterns, overall HDR and precise HDR (Fig. 4f, g). For sgRNA

758   without [C] extension, estimated h (2.07%) was used. The simulated data well fitted to the

759   experimental results (Fig. 4f, g). To predict HDR outcomes continuously, we designed

760   hypothetical function of h along P (h = 2.07% (P > 0.9); h = 10.99% (P < 0.9)) (Extended

761   Data Fig. 8d) and estimated the frequency of distinct HDR patterns, overall HDR and

762   precise HDR (Extended Data Fig. 8e, f). In the simulation, maximum of precise HDR is

763   obtained when P = 0.313 (Extended Data. Fig. 8c, f).

764

765   **Modeling of HDR-based gene correction (Figure 5)**

766   Using beta distribution, frequencies of the various HDR clones in Figure 5 are determined

767   as follows (Extended Data Fig. 8a and 10a, b):

768
$$F(WT/\,R206H\_Corrected) = \int_0^1 hP(1-P')(1-P'')f(P;\alpha,\beta)dP \qquad (22)$$

769
$$F(WT\_indel/R206H\_Corrected) = \int_0^1 h(1-h)PP'(1-P'')f(P;\alpha,\beta)dP \qquad (23)$$

770
$$F(WT\_Corrected/R206H\_Corrected) = \int_0^1 h^2 PP'(1-P'')^2 f(P;\alpha,\beta)dP \qquad (24)$$

771
$$F(WT\_Corrected\_indel/R206H\_Corrected) = \int_0^1 h^2 PP'P''(1-P'')f(P;\alpha,\beta)dP \quad (25)$$

772
$$F(WT/R206H\_Corrected\_indel) = \int_0^1 hP(1-P')P''f(P;\alpha,\beta)dP \qquad (26)$$

773
$$F(WT\_indel/R206H\_Corrected\_indel) = \int_0^1 h(1-h)PP'P''f(P;\alpha,\beta)dP \qquad (27)$$

774
$$F(WT\_Corrected/R206H\_Corrected\_indel) = \int_0^1 h^2 PP'P''(1-P'')f(P;\alpha,\beta)dP \quad (28)$$

775 $$F(WT\_Corrected\_indel/R206H\_Corrected\_indel) = \int_0^1 h^2 PP'P''^2 f(P; \alpha, \beta)dP \quad (29)$$

776 $$F(WT\_Corrected/R206H) = \int_0^1 h(1-P)P'(1-P'')f(P; \alpha, \beta)dP \quad (30)$$

777 $$F(WT\_Corrected\_indel/R206H) = \int_0^1 h(1-P)P'P''f(P; \alpha, \beta)dP \quad (31)$$

778 $$F(WT\_Corrected/R206H\_indel) = \int_0^1 h(1-h)PP'(1-P'')f(P; \alpha, \beta)dP \quad (32)$$

779 $$F(WT\_Corrected\_indel/R206H\_indel) = \int_0^1 h(1-h)PP'P''f(P; \alpha, \beta)dP \quad (33)$$

780 $$F(overall\ HDR) = \int_0^1 (-h^2 PP' + hP + hP')f(P; \alpha, \beta)dP \quad (34)$$

781 , where efficiency of HDR on Cas9-cleaved single allele and the probability of the single-

782 gene editing on WT or HDR-corrected target, i.e. 1mm or 2mm target, are defined as h and

783 P´ or P´´, respectively (Extended Data Fig. 10a). P´ and P´´ is described in the same manner

784 to equation (12):

785 $$P' = \frac{P}{(1-m_1)P + m_1} \quad (35)$$

786 $$P'' = \frac{P}{(1-m_2)P + m_2} \quad (36)$$

787 , where m1 is 3.459 and m2 is 12.0793, respectively (Extended Data Fig. 7). The

788 relationship between [C] extension and P is shown in Fig. 5c and Extended Data. Fig. 10b.

789 For simplicity, h was considered to be constant across cell population for

790 each experiment. In addition, HDR rate on R206H and WT allele was considered to be

791 same. Based on the experimental results of overall HDR frequencies and the equation (eq.

792 #34), h was estimated for each [C] extended sgRNA (Fig. 5h). Consistent with the results

793   in Fig. 4, h with [C] extension was higher than h without [C] extension. Together with the

794   results in Fig. 4, this suggests that conventional system without [C] extension reduces HDR

795   probably due to extensive DNA damage and p53 response (as examined in Fig. 5d, e) and

796   [C] extension releases the suppression to the upper limit of HDR. We also observed that h

797   in Fig. 5 was generally higher than h in Fig. 4. This may be because cell lines used in Fig.

798   5 have only one perfect match target, thus eliciting weaker suppressive effects on HDR

799   rate, while cell lines used in Fig. 4 have two perfect match targets. Based on these findings,

800   we used mean of estimated h (26.93%) as the h for [C] extended sgRNAs and estimated

801   the frequency of overall HDR and precise HDR (Fig. 5i and Extended Data Fig. 10c). For

802   sgRNA without [C] extension, estimated h (13.21%) was used. The simulated data well

803   fitted to the experimental results (Fig. 5i and Extended Data Fig. 10c). To predict HDR

804   outcomes continuously, we designed hypothetical function of h along P (h = 13.21% (P >

805   0.9); h = 26.93% (P < 0.9)) (Extended Data Fig. 10d) and estimated the frequency of

806   distinct HDR patterns, overall HDR and precise HDR (Extended Data Fig. 10e). In the

807   simulation, maximum of precise HDR is obtained when P = 0.424 (Extended Data. Fig.

808   10b, e).

809

810   **Statistics**

811   Sample sizes were determined based on our previous experience of performing similar sets

812   of experiments. Statistical tests were performed using JMP (14.2.0) and R (3.2.1). We

813   verified the equality of variance assumption by using the F-test or Levene test. As a pre-

814   test of normality, we used the Kolmogorov–Smirnov test. Differences between two groups

815   were analyzed using two-tailed Student's t-test (Fig. 2e) or Welch's t-test (Fig. 2h, right).

816   Comparisons among more than two groups were analyzed using one-way or two-way

817   ANOVA and post hoc Tukey–Kramer test (Fig. 2g, 4d, and Extended Data Fig. 5b, e, f) or

818   Welch's test with post hoc Games–Howell test (Fig. 1g, 2a, 5d, e, and Extended Data Fig.

819   9b, d, f, h). In all bar graphs, data are expressed as mean ± s.e.m. (Fig. 2g, h, 4d, 5f, and

820   Extended Data Fig. 1d, 5a-c, e, f) or ± s.d. (Fig. 2a, 5d, e, g, and Extended Data Fig. 9b, d,

821   f and h). In the scatter dot plots, center lines show medians; whiskers show 25th and 75th

822   percentiles from median (Fig. 1g). In the box plots, center lines show medians; box limits

823   indicate the 25th and 75th percentiles; whiskers range from a minimum to a maximum

824   value (Fig. 2e).

825

826   **Data availability**

827   All data will be made available upon request to the corresponding author.

828

829   **Code availability**

830   Scripts needed to reconstruct analysis files will be made available on request.

831

832

833   **Methods References**

834   39   Yagi, M. *et al.* Derivation of ground-state female ES cells maintaining gamete-
835   derived DNA methylation. *Nature* **548**, 224-227, doi:10.1038/nature23286 (2017).
836   40   Okita, K. *et al.* A more efficient method to generate integration-free human iPS
837   cells. *Nat Methods* **8**, 409-412, doi:10.1038/nmeth.1591 (2011).
838   41   Srinivas, S. *et al.* Cre reporter strains produced by targeted insertion of EYFP and
839   ECFP into the ROSA26 locus. *BMC Dev Biol* **1**, 4, doi:10.1186/1471-213x-1-4
840   (2001).
841

842

859   **AUTHOR CONTRIBUTIONS**

860   M.K. conceived and designed the research. M.K. and R.K. performed experiments. M.K

861   and H.I.S. analyzed data. H.I.S performed computational analysis. M.K., H.I.S. and A.S.

862   wrote the manuscript. All authors read and approved the final manuscript. A.S. supervised

863   the project.

864

865   **Competing interests**

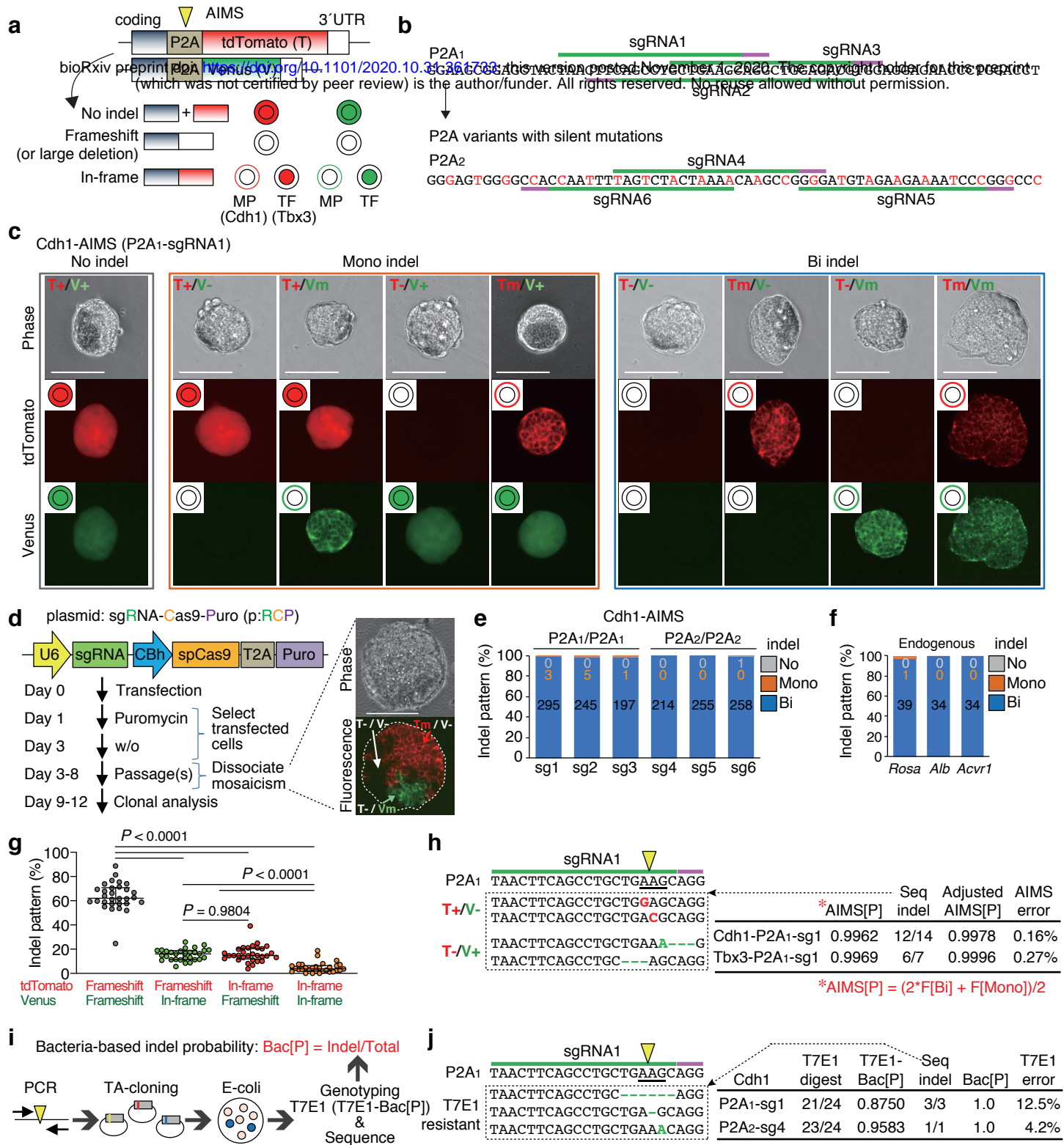866   The authors declare no competing interests.

Figure 1

Kawamata et al.

a

coding | AIMS | 3´UTR
P2A | tdTomato (T)

No indel + = (red) (green)
Frameshift (or large deletion)
In-frame
MP (Cdh1) | TF (Tbx3) | MP | TF

b

sgRNA1 · sgRNA3
sgRNA2

P2A variants with silent mutations

P2A2
GGGAGTGGGGCCACCAATTTTAGTCTACTAAAACAAGCCGGGGATGTAGAAGAAAATCCCGGGCCC
sgRNA4
sgRNA6 · sgRNA5

c Cdh1-AIMS (P2A1-sgRNA1)

No indel | Mono indel | Bi indel
T+/V+ | T+/V- | T+/Vm | T-/V+ | Tm/V+ | T-/V- | Tm/V- | T-/Vm | Tm/Vm

Phase / tdTomato / Venus

d plasmid: sgRNA-Cas9-Puro (p:RCP)

U6 — sgRNA — CBh — spCas9 — T2A — Puro

Day 0 Transfection
Day 1 Puromycin — Select transfected cells
Day 3 w/o
Day 3-8 Passage(s) — Dissociate mosaicism
Day 9-12 Clonal analysis

Phase / Fluorescence: T-/V-, Tm/V-, T-/Vm

e Cdh1-AIMS

P2A1/P2A1 | P2A2/P2A2

indel: No / Mono / Bi

	sg1	sg2	sg3	sg4	sg5	sg6
No	0	0	0	0	0	1
Mono	3	5	1	0	0	0
Bi	295	245	197	214	255	258

f Endogenous

indel: No / Mono / Bi

	Rosa	*Alb*	*Acvr1*
No	0	0	0
Mono	1	0	0
Bi	39	34	34

g

P < 0.0001
P < 0.0001
P = 0.9804

tdTomato/Venus:
Frameshift/Frameshift | Frameshift/In-frame | In-frame/Frameshift | In-frame/In-frame

h

sgRNA1
P2A1 TAACTTCAGCCTGCTG**AAG**CAGG

T+/V-
TAACTTCAGCCTGCTG**G**GCAGG
TAACTTCAGCCTGCTGA**C**GCAGG

T-/V+
TAACTTCAGCCTGCTGAAA**A**---G
TAACTTCAGCCTGC---AGCAGG

	*AIMS[P]	Seq indel	Adjusted AIMS[P]	AIMS error
Cdh1-P2A1-sg1	0.9962	12/14	0.9978	0.16%
Tbx3-P2A1-sg1	0.9969	6/7	0.9996	0.27%

*AIMS[P] = (2*F[Bi] + F[Mono])/2

i Bacteria-based indel probability: Bac[P] = Indel/Total

PCR → TA-cloning → E-coli → Genotyping T7E1 (T7E1-Bac[P]) & Sequence

j

sgRNA1
P2A1 TAACTTCAGCCTGCTG**AAG**CAGG

T7E1 resistant
TAACTTCAGCCTGC-----AGG
TAACTTCAGCCTGCTGA-GCAGG
TAACTTCAGCCTGCTGAA**A**CAGG

Cdh1	T7E1 digest	T7E1-Bac[P]	Seq indel	Bac[P]	T7E1 error
P2A1-sg1	21/24	0.8750	3/3	1.0	12.5%
P2A2-sg4	23/24	0.9583	1/1	1.0	4.2%

Fig. 1. Visualization of allele-specific genome editing events by AIMS.
a, Schematic of AIMS. A mESC clone harboring dual color reporters is generated by fusing P2A-fluorescence cassettes at the ends of coding regions of target genes. P2A is targeted by sgRNA-Cas9 (yellow arrowhead). TF, Transcription factor; MP, Membrane protein. **b,** Target sequences of sgRNAs in the P2A1 and P2A2 are shown. The original P2A is denoted as P2A1, and the variant generated by silent mutations (red) is denoted as P2A2. **c,** Representative results of Cdh1-P2A1-AIMS. Genotypes are determined by nine combinations of tdTomato/Venus expression and localization. T, tdTomato; V, Venus; +, no indel; m, in-frame indel represented by membrane localization; -, frameshift indel or large deletion represented by loss of fluorescence. Scale bar indicates 100 μm. **d,** Schematic description of protocol for genome editing using all-in-one CRISPR plasmids (pRCP, sgRNA-Cas9-Puro). The images show mosaicism in a single cell-derived primary puromycin-resistant colony. Scale bar indicates 100 μm. **e,** Indel patterns are measured by Cdh1-P2A1-AIMS and Cdh1-P2A2-AIMS. sg1-6, sgRNAs1-6 shown in Fig. 1b. Data are shown as mean from n = 3 independent experiments performed at different times, except for sg1 (*n* = 6). Total number of clones analyzed is shown in each column (also in **f**). **f,** Indel patterns for the endogenous genes are determined by sequence analysis at the clonal level. Data are shown as mean from *n* = 3 independent experiments performed at different times. **g,** Percentages of the four types of bi-allelic indel patterns are shown. Dots indicate individual data points (*n* = 30, 6 sgRNAs, Tbx3- and Cdh1-AIMS) and median with interquartile range are shown. Statistical significance is assessed using Welch's test with post hoc Games–Howell test. **h,** Representative indel sequences in the P2A1 region of tdTomato or Venus allele in the T+/V- or T-/V+ clones, respectively (left) and AIMS error rates (right) are shown. AIMS[P], the value of indel probability calculated from frequency (F) of bi-allelic [Bi] and mono-allelic [Mono] indel clones. The formula is shown in red below. Seq-indel, the exact number of bi-allelic indel clones with a phenotype of T+/V- or T-/V+ is determined by sequencing the tdTomato or Venus allele, respectively. Adjusted AIMS[P], indel probability considering the Seq-indel data. AIMS error, the values of Adjusted AIMS[P] minus AIMS[P]. **i,** Schematic description of the procedure for calculating bacteria-based indel probabilities (Bac[P]). **j,** Representative T7E1-insensitive indel sequences (left) and the error rate of the T7E1 assay (right) are shown. T7E1-Bac[P], indel probability calculated from the rate of clone number sensitive to T7E1 digestion. Seq-indel, the exact number of indel clones is determined by sequencing the PCR products which are not digested by T7E1. Bac[P], indel probability considering the Seq-indel data. T7E1 error, the values of Bac[P] minus T7E1-Bac[P]. Arrowheads and underlines indicate the position of the DSB sites and codon, respectively (**h, j**).
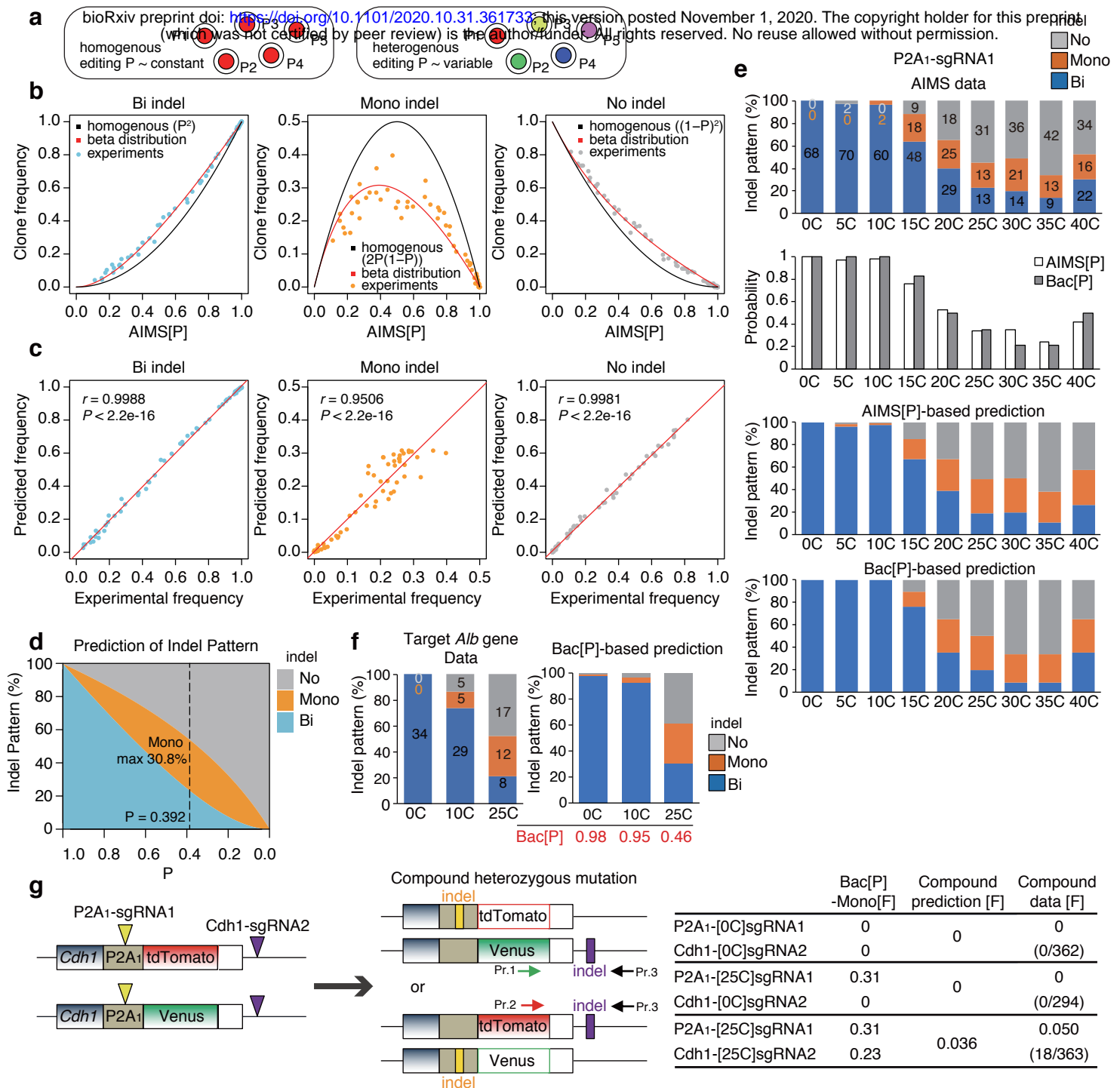
Figure 2
Kawamata et al.

Fig. 2. Downsizing of sgRNA-Cas9 activity by addition of 5'-end cytosine stretches.

a, Analysis of indel patterns (left) and colony numbers (right) after transfecting all-in-one plasmids containing sgRNA1 at different concentrations in Tbx3-P2A1-AIMS. pRCP, all-in-one plasmid shown in Fig.1d. Data are shown as mean and s.d. from $n = 4$ biological replicates. Total number of clones is shown in each column (also in **c** and **d**). Statistical significance is assessed using Welch's test with post hoc Games–Howell test. **b,** Schematic of nucleotide extension at the 5' end of spacer for downsizing sgRNA-Cas9 activity. **c,** Effects of 15-base cytosine [15C], guanine [15G], adenine [15A], and thymidine [15T] extension for sgRNA1 in Cdh1-P2A1-AIMS. Data are shown as mean from $n = 3$ independent experiments performed at different times. **d,** Indel pattern analysis using 6 different sgRNAs in Cdh1-P2A1-AIMS and Cdh1-P2A2-AIMS. Data are shown as mean from $n = 3$ independent experiments performed at different times. **e,** Percentage of mono-allelic indel frequencies for the tdTomato and Venus alleles. Dots indicate individual data points ($n = 73$, 6 sgRNAs, Tbx3- and Cdh1-AIMS). In the box plots with interquartile range, the center lines show medians, and whiskers range from a minimum to a maximum value. Statistical significance is assessed using two-tailed Student's t-test. **f,** An in vitro cleavage assay to compare [0C], [10C] and [25C]sgRNAs for DSB induction potential. PCR amplicons (951 bp) containing a Tbx3-P2A1-sgRNA1 targeting site is digested by ribonucleoprotein (RNP) composed of [C]sgRNA and SpCas9 recombinant protein. Asterisks indicate digested products (741 bp and 210 bp). **g,** Mosaic frequency before and after passage using different [C]sgRNAs in Cdh1-P2A1-AIMS. Data are shown as mean ± s.e.m. from $n = 3$ independent experiments performed at different times. Statistical significance is assessed using two-way ANOVA and post hoc Tukey–Kramer test. **h,** Induction of mono-allelic HDR without induction of indels on a non-HDR allele. A schematic of HDR of a P2A1-tdTomato cassette at the end of *Tbx3* coding site (left). T7E1 assay to survey indel probability induced by [C]sgRNAs (second from the left). Frequencies of overall HDR (second from the right) and scarless HDR (right) are shown as mean ± s.e.m. from $n = 4$ and $n = 5$ independent experiments, respectively, which are performed at different times. Statistical significance for scarless HDR frequency (right) is assessed using Welch's t-test. Arrowheads indicate DSB sites. Asterisks indicate PCR products digested by T7E1. N, PX459 plasmid without spacer.

Figure 3

Kawamata et al.

Fig. 3. Computational prediction of single-cell heterogeneity of genome editing and bi-/mono-allelic indel frequency.
a, Homogeneity vs heterogeneity of genome editing frequency at the single cell level. **b,** Relationships between AIMS[P] and clone frequency for Bi-, Mono-, or No indel ($n = 64$). The two curves are generated based on the assumption that single-cell editing probability is homogenous or heterogeneous. In a latter case, beta distribution is adopted. **c,** Correlation between experimental data and beta distribution-based prediction of the frequencies or Bi-, Mono-, or No indel. Linear regression and Pearson's correlation coefficients (r) with P-values are shown. **d,** Relationships between indel probability (P) and indel pattern, simulated by the beta distribution model. The maximum frequency (30.8 %) of mono-allelic indel is obtained when setting P to 0.392. **e,** Comparison between AIMS experimental results with Cdh1-P2A1-sgRNA1 and predictions based on AIMS[P] and Bac[P]. Data are shown as mean from $n = 3$ independent experiments performed at different times and total number of clones analyzed are shown in each column in the AIMS data. **f,** Comparison between experimental data and Bac[P]-based prediction for indel pattern when targeting an endogenous *Alb* (*Albumin*) gene. Data are shown as mean ± s.e.m. from $n = 3$ independent experiments performed at different times and total number of clones analyzed are shown in each column. **g,** Prediction and generation of compound heterozygous mutation clones using Cdh1-P2A1-AIMS. Bac[P]-Mono[F], frequency of mono-allelic indel (Mono[F]) predicted from Bac[P]. Brackets indicate the number of compound heterozygous mutation clones generated by $n = 3$ independent experiments performed at different times. Yellow and purple arrowheads and boxes indicate DSB sites and indels, respectively. Pr.1-3, primers for genotyping.

Figure 4
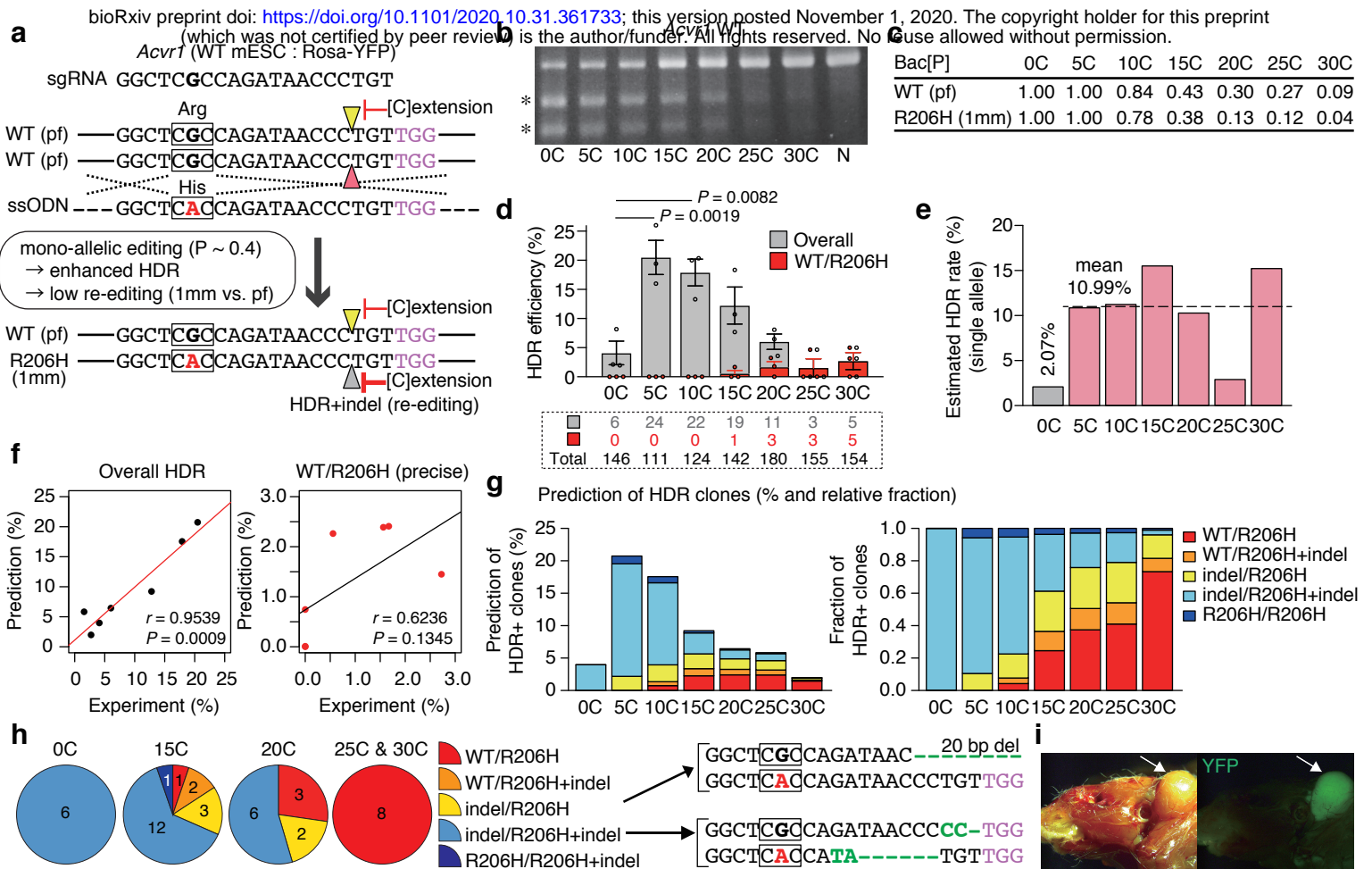
Fig. 4. Generation of a heterozygous FOP disease model.
a, Schematic of precise HDR for mono-allelic G>A replacement without indels on both HDR and non-HDR alleles in *Acvr1* gene in mESCs. Arrowheads indicate DSB sites. Squares indicate a codon. pf, perfect match; 1mm, 1 bp mismatch. **b,** T7E1 assay. Asterisks indicate PCR products digested by T7E1. N, PX459 plasmid without spacer. **c,** Bac[P] values for both WT and R206H alleles. **d,** Clonal analysis of overall HDR and precise HDR (WT/R206H) efficiencies in the WT/WT mESCs. Overall HDR comprises precise HDR and other HDRs with indels in the HDR- and/or non-HDR-alleles. The number of clones analyzed is shown in a dotted square. Data are shown as mean ± s.e.m. from *n* = 3 independent experiments performed at different times. Statistical significance for overall HDR is assessed using one-way ANOVA and post hoc Tukey–Kramer test. **e,** Computational estimation of HDR rates at single allele. **f,** Correlation between experimental and computationally predicted HDR frequencies. Overall (left) and precise WT/R206H HDR (right) are shown. Linear regression and Pearson's correlation coefficients (*r*) with P-values are shown. **g,** Prediction of diverse HDR events (left) and relative fraction (right). **h,** Detailed distribution of HDR events shown in the Fig. 4d is shown with actual clone number. Representative sequences of indel/R206H and indel/R206H+indel clones are shown. Squares indicate codon. **i,** FOP mouse model is generated by microinjection of a WT/R206H clone. An arrow indicates an area of ectopic ossification with mESC contribution, which is traced by the Rosa-YFP reporter.

Figure 5
Kawamata et al.
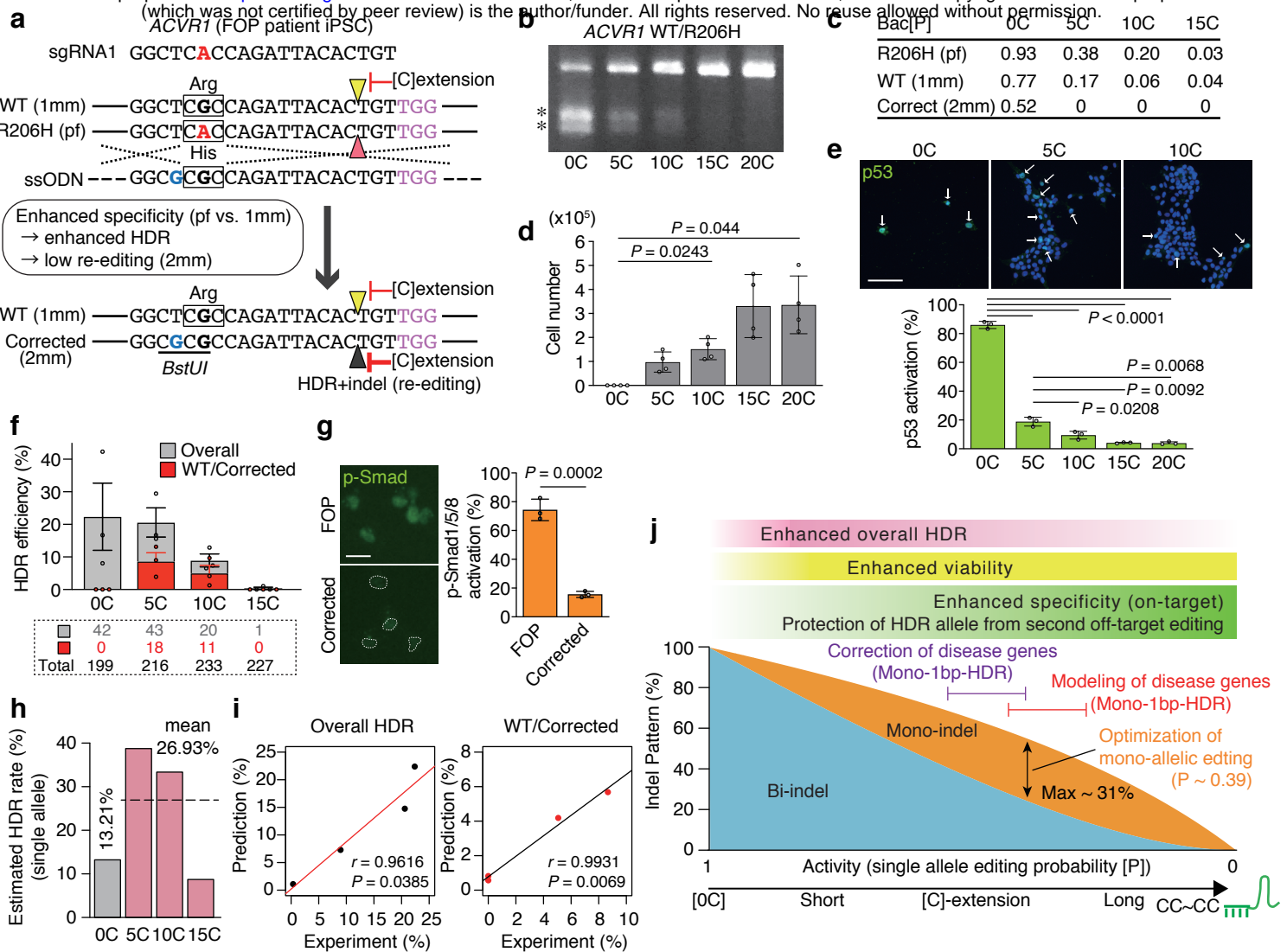
Fig. 5. Safe and systematic precise gene correction in FOP hiPSCs.

a, Schematic of R206H allele-selective precise HDR for A>G correction in FOP iPSCs (WT/R206H). Silent mutation of guanine (G, blue) creates a *BstUI* restriction enzyme site, which allows for rapid selection of HDR clones and for discriminating the Corrected allele (2mm) from original WT one (1mm). Arrowheads indicate DSB sites. Squares indicate codon. pf, perfect match; 1mm, 1 bp mismatch; 2mm, 2 bp mismatches. **b,** T7E1 assay. Asterisks indicate PCR products digested by T7E1. N, PX459 plasmid without spacer. **c,** Bac[P] values for R206H (pf), WT (1mm) and Corrected (2mm) alleles. **d,** Cytotoxicity is examined by counting cell number after all-in-one plasmid transfection and puromycin selection. Data are shown as mean and s.d. from $n = 4$ biological replicates. Statistical significance is assessed using Welch's test with post hoc Games–Howell test. **e,** Immunocytochemistry to examine p53 activation in the FOP hiPSCs. Data are shown as mean and s.d. from $n = 3$ biological replicates. Statistical significance is assessed using Welch's test with post hoc Games–Howell test. **f,** Clonal analysis of overall HDR and precise HDR (WT/Corrected) efficiencies in the FOP hiPSCs (WT/R206H). Overall HDR comprises R206- and/or WT-allele-HDR with or without indels. The number of clones analyzed is shown in a dotted square. Data are shown as mean ± s.e.m. from $n = 3$ independent experiments performed at different times. **g,** Immunocytochemistry to examine Activin-induced pSmad1/5/8 activation in the FOP (WT/R206H) hiPSCs and a corrected (WT/Corrected) clone. Data are shown as mean and s.d. from $n = 3$ biological replicates. Statistical significance is assessed using two-tailed Student's t-test. **h,** Computational estimation for HDR rate at single allele. **i,** Correlation between experimental HDR frequencies and computational modeling. Overall (left) and precise WT/Corrected HDR (right) are shown. Linear regression and Pearson's correlation coefficients (r) with P-values are shown. **j,** Summary of [C] extension methods.
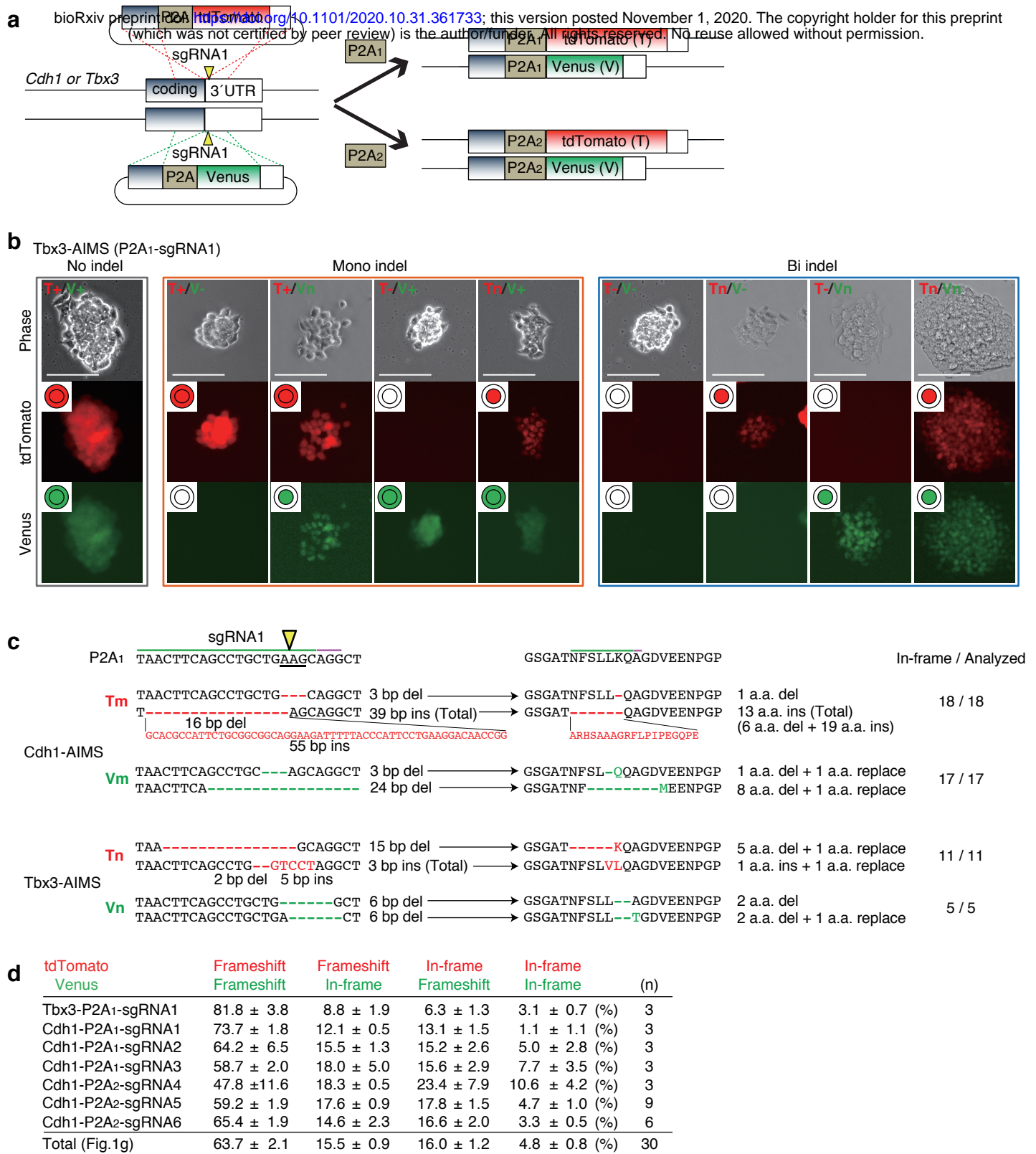
Extended Data Fig. 1. AIMS construction and indel analysis.

a, Schematic of generating dual color KI mESC clones for AIMS. Two types of targeting plasmids are simultaneously knocked into the two alleles of the *Cdh1* or *Tbx3* locus using CRISPR-Cas9. Arrowheads indicate DSB sites. **b,** Representative results of Tbx3-P2A1-AIMS. Genotypes are determined by nine combinations of tdTomato/Venus expression and localization in Tbx3-P2A1-AIMS. T, tdTomato; V, Venus; +, no indel represented by both cytosolic and nuclear localization; n, in-frame indel represented by nuclear localization; -, frameshift indel or large deletion represented by loss of fluorescence. Scale bar indicates 100 μm. **c,** Representative DNA and amino acid sequences of in-frame indels. The clones showing cytosolic expression (T+ or V+) are sequenced and the number of clones with in-frame indel are shown. **d,** The table shows percentages of the four types of bi-allelic indel patterns. Total indicates the mean of all data (*n* = 30), which is shown in Fig. 1g. Data are shown as mean ± s.e.m..
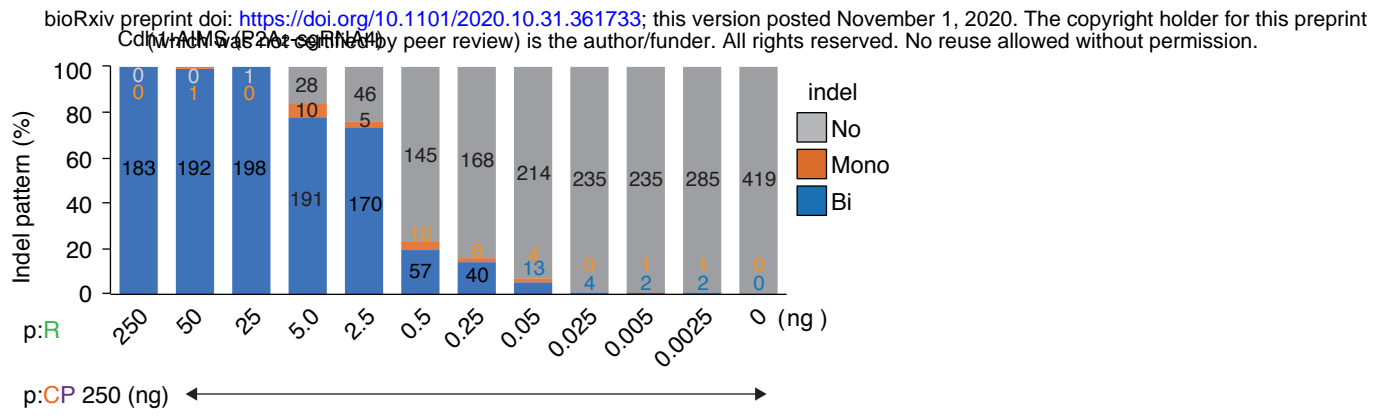
Extended Data Fig. 2. A minor effect of plasmid reduction on mono-allelic indel induction.
Indel pattern is analyzed using Cdh1-P2A2-AIMS. The spacerless-PX459 plasmid (p:CP, 250 ng) is co-transfected with different amounts of the P2A2-sgRNA4 sgRNA expression plasmid (p:R). Data are shown as mean ± s.e.m. from $n = 3$ independent experiments performed at different times and total colony number analyzed is shown in each column.
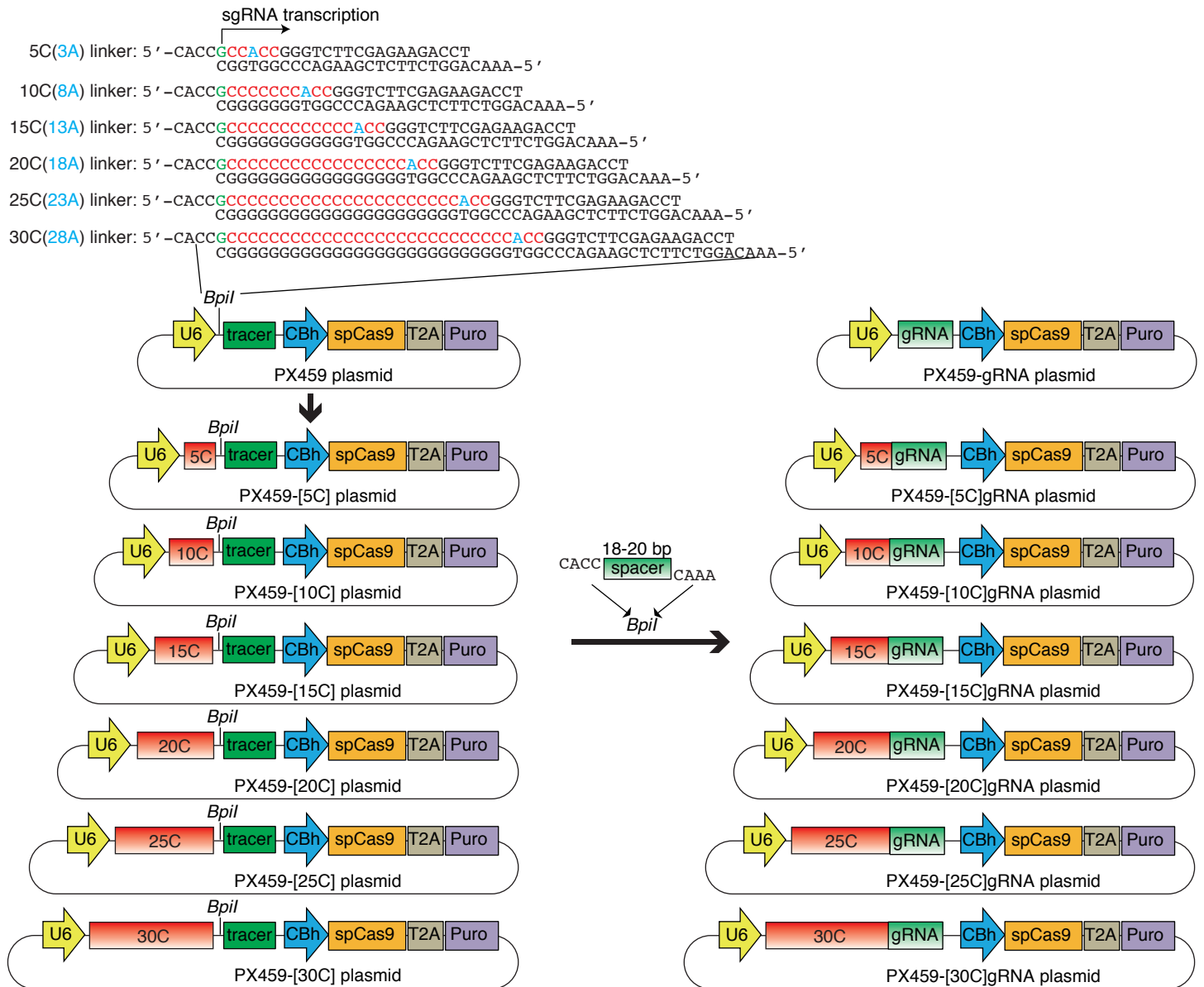
Extended Data Fig. 3. Construction of [0C]-[30C]sgRNA expressing all-in-one plasmids.

The linkers are inserted into the *BpiI* site of the PX459 plasmid. Adenine (A, blue) is inserted at the third position from the 3' end of the cytosine extension to create an overhang sequence for insertion of spacer sequences with CCAC overhang. The [5C]-[30C]sgRNA-expressing all-in-one plasmids can be produced by inserting a standard 18-20 bp spacer linker between two *BpiI* sites.

a

b

c
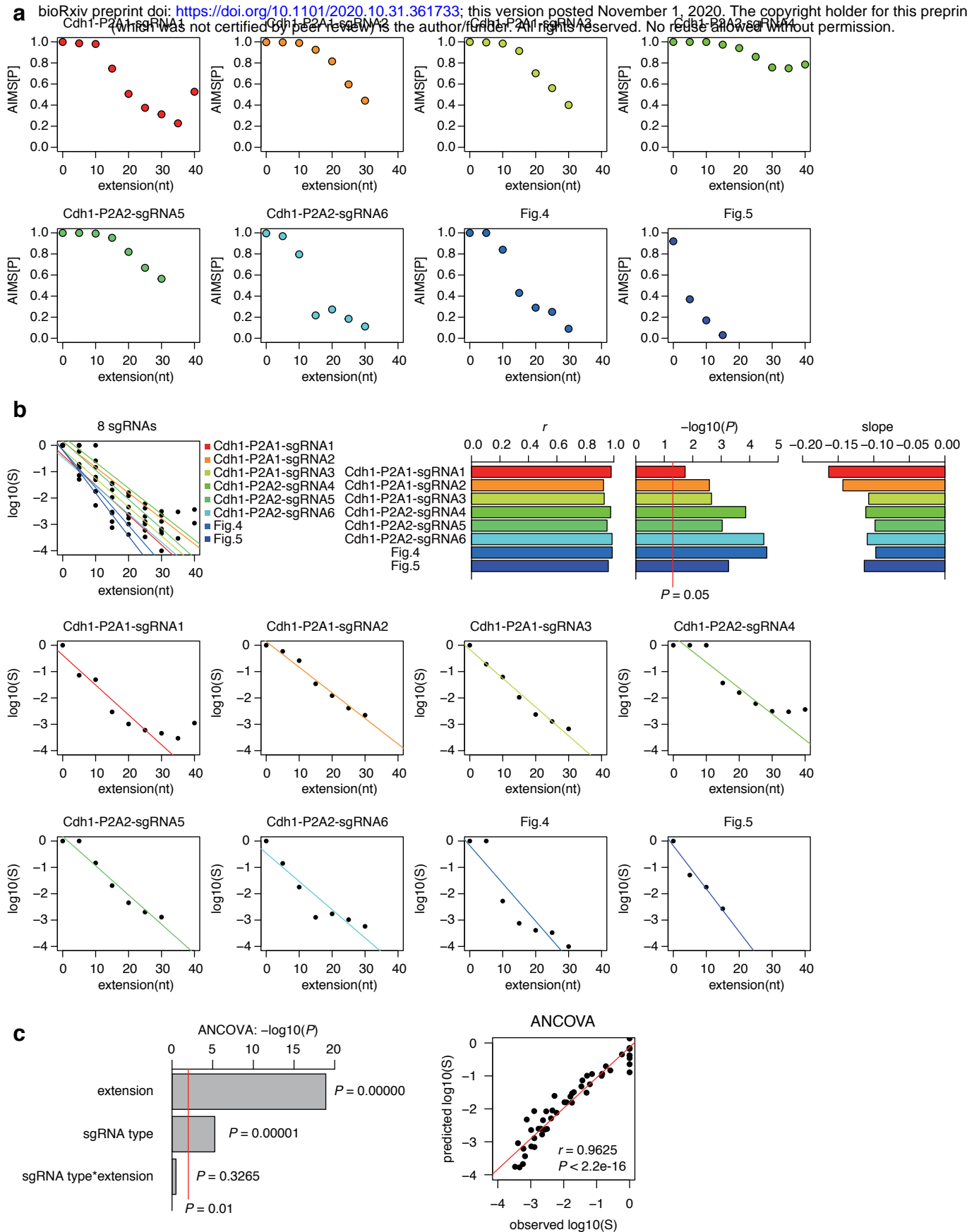
Extended Data Fig. 4. Quantitative assessment of the suppressive effects of [C] extension for different sgRNAs.
a, Relationships between [C] extension length and AIMS[P] are shown for 8 sgRNA. **b,** Relationships between [C] extension length and concentration of effective sgRNA-Cas9 complex (log10(S)) are shown. The three upper right panels show the results of linear regression analysis, including Pearson's correlation coefficients (*r*), P-values, and slopes. The upper left panels and 8 bottom panels show the correlation between [C] extension length and log10(S) for all sgRNAs (overlayed) and each sgRNA, respectively. Note that 8 sgRNAs have similar slope values, suggesting uniform effects of [C] extension. **c,** ANCOVA (analysis of covariance) analysis to investigate the differences of slope values for 8 sgRNAs. Statistical results for each source of variance are shown in left. Right panel shows a correlation between observed and predicted log10(S). Linear regression and Pearson's correlation coefficient (*r*) with P-value are shown.

Extended Data Figure 5

a

	tdTomato / Venus		(n)
	Indel (+) / Indel (−)	Indel (−) / Indel (+)	
Tbx3-P2A1-sgRNA1	46.6 ± 3.6	53.4 ± 3.6 (%)	12
Cdh1-P2A1-sgRNA1	53.7 ± 3.2	46.3 ± 3.2 (%)	17
Cdh1-P2A1-sgRNA2	53.0 ± 5.2	47.0 ± 5.2 (%)	8
Cdh1-P2A1-sgRNA3	47.4 ± 5.4	52.6 ± 5.4 (%)	9
Cdh1-P2A2-sgRNA4	45.2 ± 4.7	54.8 ± 4.7 (%)	7
Cdh1-P2A2-sgRNA5	44.2 ± 5.0	55.8 ± 5.9 (%)	9
Cdh1-P2A2-sgRNA6	44.6 ± 4.5	55.4 ± 4.5 (%)	11
Total (Fig. 2e)	48.3 ± 1.6	51.7 ± 1.6 (%)	73
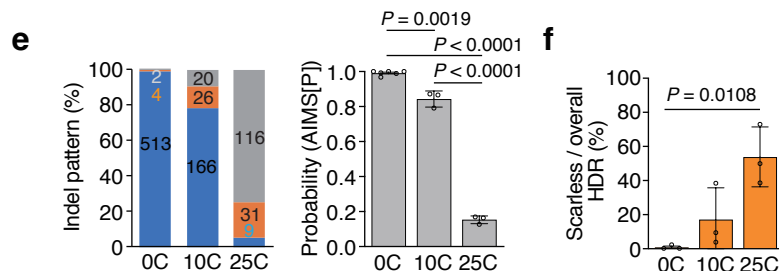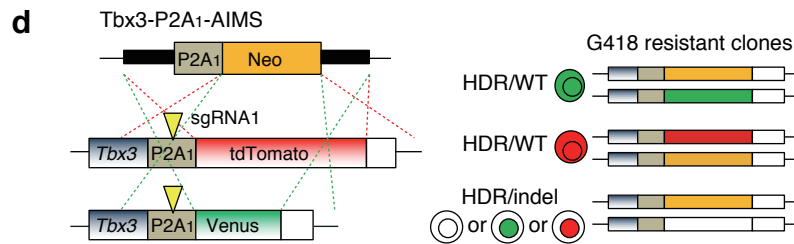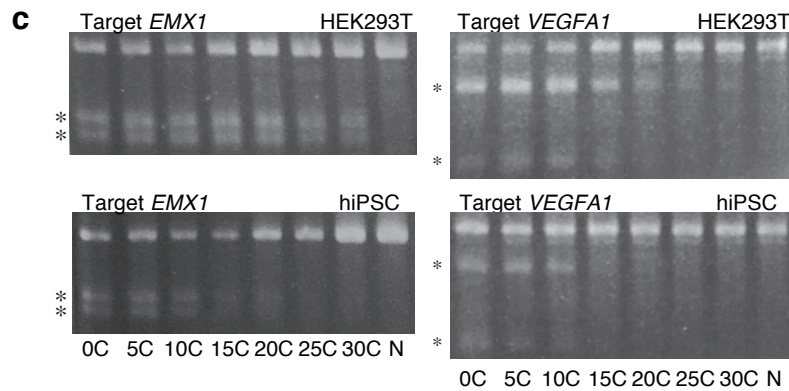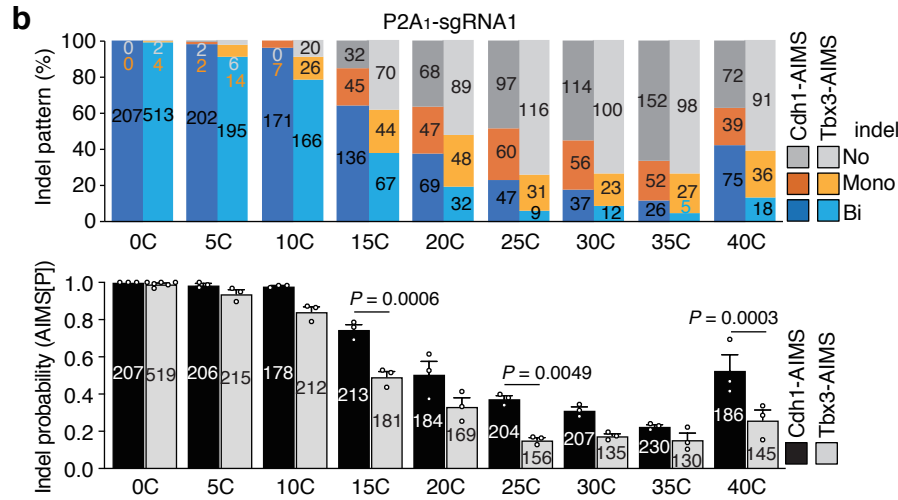
Extended Data Fig. 5. Additional results of AIMS experiments.
a, The table shows percentages of the two types of mono-allelic indel patterns. Total indicates the mean of all data ($n = 73$), which is shown in the Fig. 2e. Data are shown as mean ± s.e.m.. **b,** Different indel frequency at different chromosomal loci. Indel pattens and probabilities (AIMS[P]) are compared between Cdh1-P2A1-AIMS and Tbx3-P2A1-AIMS. The data for the indel pattern of Cdh1-AIMS (P2A1-sgRNA1) were from Fig. 2d. Data are shown as mean ± s.e.m. from $n = 3$ (0C in Tbx3-AIMS, $n = 6$) independent experiments performed at different times and total colony number is shown in each column. Statistical significance is assessed using two-way ANOVA and post hoc Tukey–Kramer test. **c,** Comparison of indel probability between HEK293T cells and hiPSCs. Asterisks indicate PCR products digested by the T7E1 assay. N, PX459 plasmid without spacer. **d,** Schematic of measuring the frequency of scarless mono-allelic HDR without indels on the non-HDR allele using Tbx3-P2A1-AIMS. Arrowheads indicate DSB sites. **e,** Indel pattern (left) and probability (AMIS[P], right) are shown. The data of the indel pattern of Tbx3-AIMS (P2A1-sgRNA1) are from Extended Data Fig. 5b. Data are shown as mean ± s.e.m. from $n = 3$ independent experiments performed at different times and total colony number is shown in each column. Statistical significance is assessed using one-way ANOVA and post hoc Tukey–Kramer test. **f,** Frequencies of scarless HDR are shown as mean ± s.e.m. from $n = 3$ independent experiments performed at different times. Statistical significance is assessed using one-way ANOVA and post hoc Tukey–Kramer test.
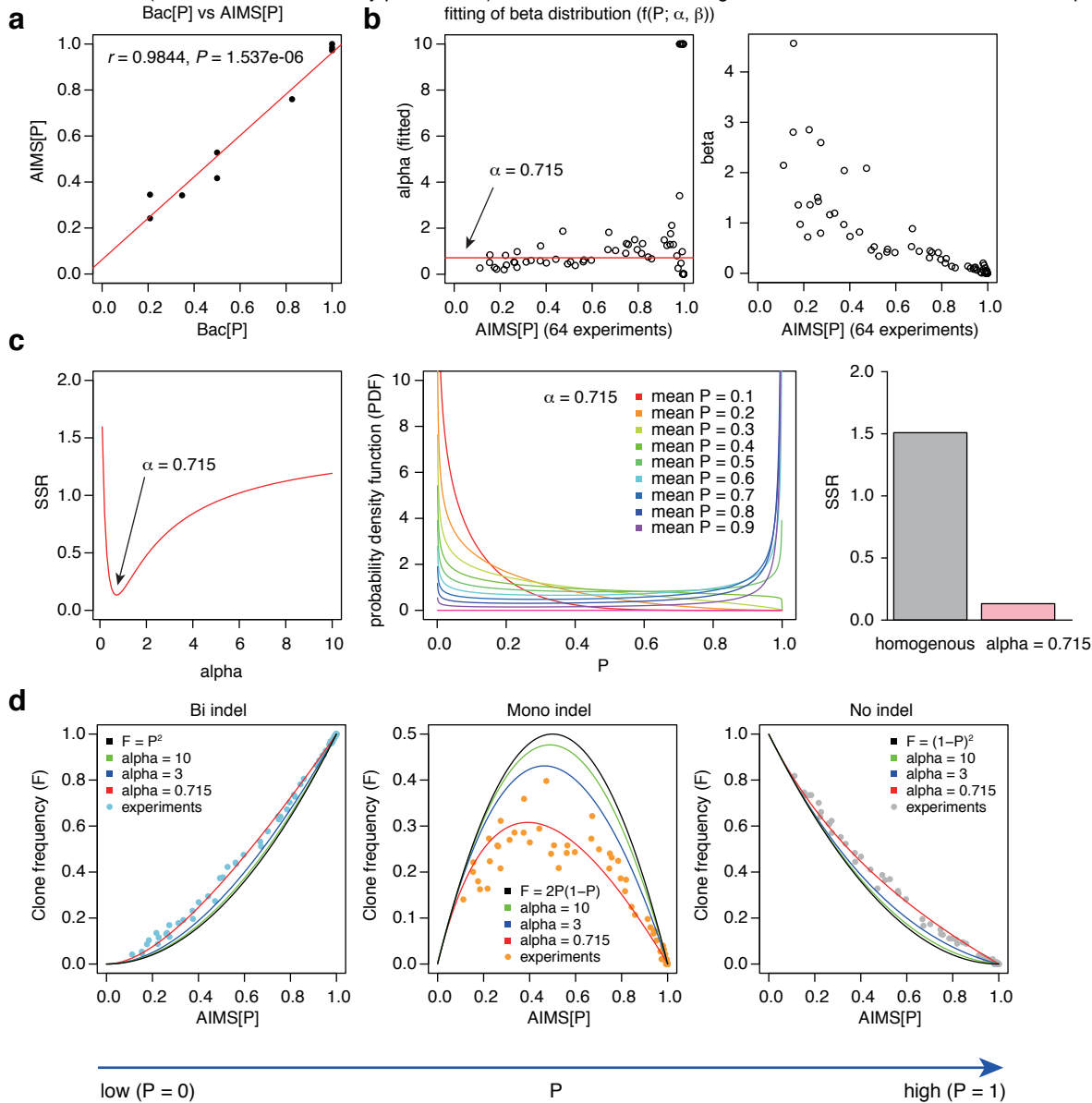
Extended Data Fig. 6. Computational modeling of single-cell heterogeneity of genome editing frequency using beta distribution.
**a,** Correlation between Bac[P] and AIMS[P] shown in Fig. 3e. Linear regression and Pearson's correlation coefficient (*r*) with P-value are shown. **b,** α and β values of beta distribution for each experiment that minimized sum of squared residuals (SSR) between experimental F(Bi), F(Mono), and F(No) and simulated F(Bi), F(Mono), and F(No). **c,** Identification of fixed α value that minimized SSR (left). Probability density functions with different mean P are shown in a middle panel. Right panel shows comparison of SSR based on the assumption that single-cell editing probability is homogenous or heterogeneous. **d,** Correlation between the experimental data and prediction of clone frequency for bi-, mono-, or no-indel. Black line is based on the assumption that genome editing probability is homogenous across the cell population. For the beta distribution, additional simulations in the case that α is 3 or 10 are also exhibited.

a

b

c

d
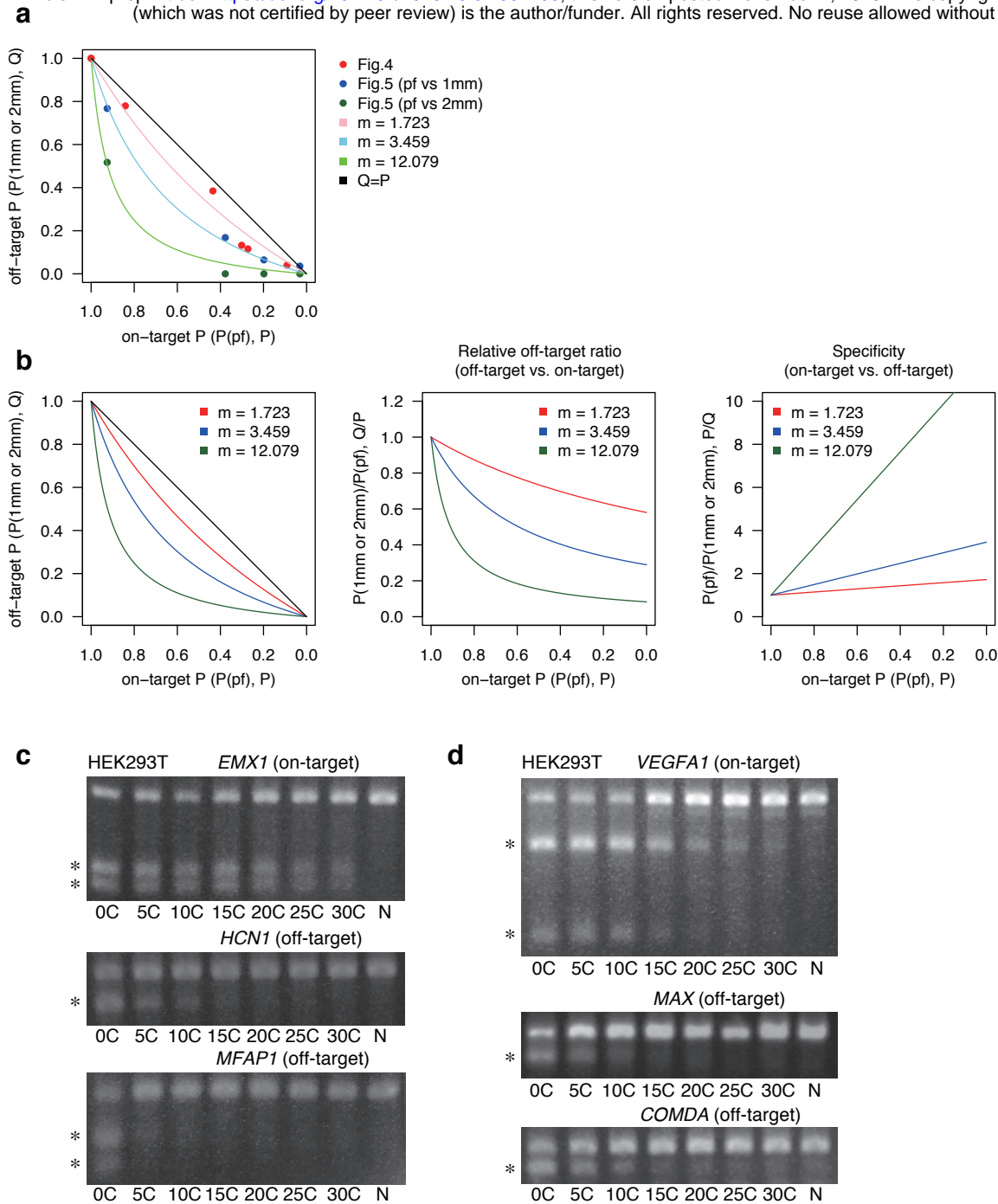
Extended Data Fig. 7. Downsizing sgRNA-Cas9 activity enhances on-target specificity and suppresses off-target effects.
**a,** Relationships between on-target editing probability on perfect match target (P) and off-target probability on 1mm or 2mm target (Q) shown in Fig. 4c and Fig. 5c. Results of computational fitting are also shown. Red, blue, and green dots indicate experimental data from Fig. 4c, Fig. 5c (pf vs 1mm), and Fig. 5c (pf vs 2mm), respectively. Details of generating simulation curves are described in Methods. **b,** Computational analysis of decrease in relative off-target editing and increase in on-targeting specificity along with reduction in indel probability. pf, perfect match; 1mm, 1 bp mismatch; 2mm, 2 bp mismatch. **c, d,** Indel probability of other sgRNAs in HEK293T cells. The T7E1 assay is performed to investigate on-target and off-target indel probability for *EMX1* (**c**) and *VEGFA1* (**d**) targeting sgRNAs.

Extended Data Figure 8
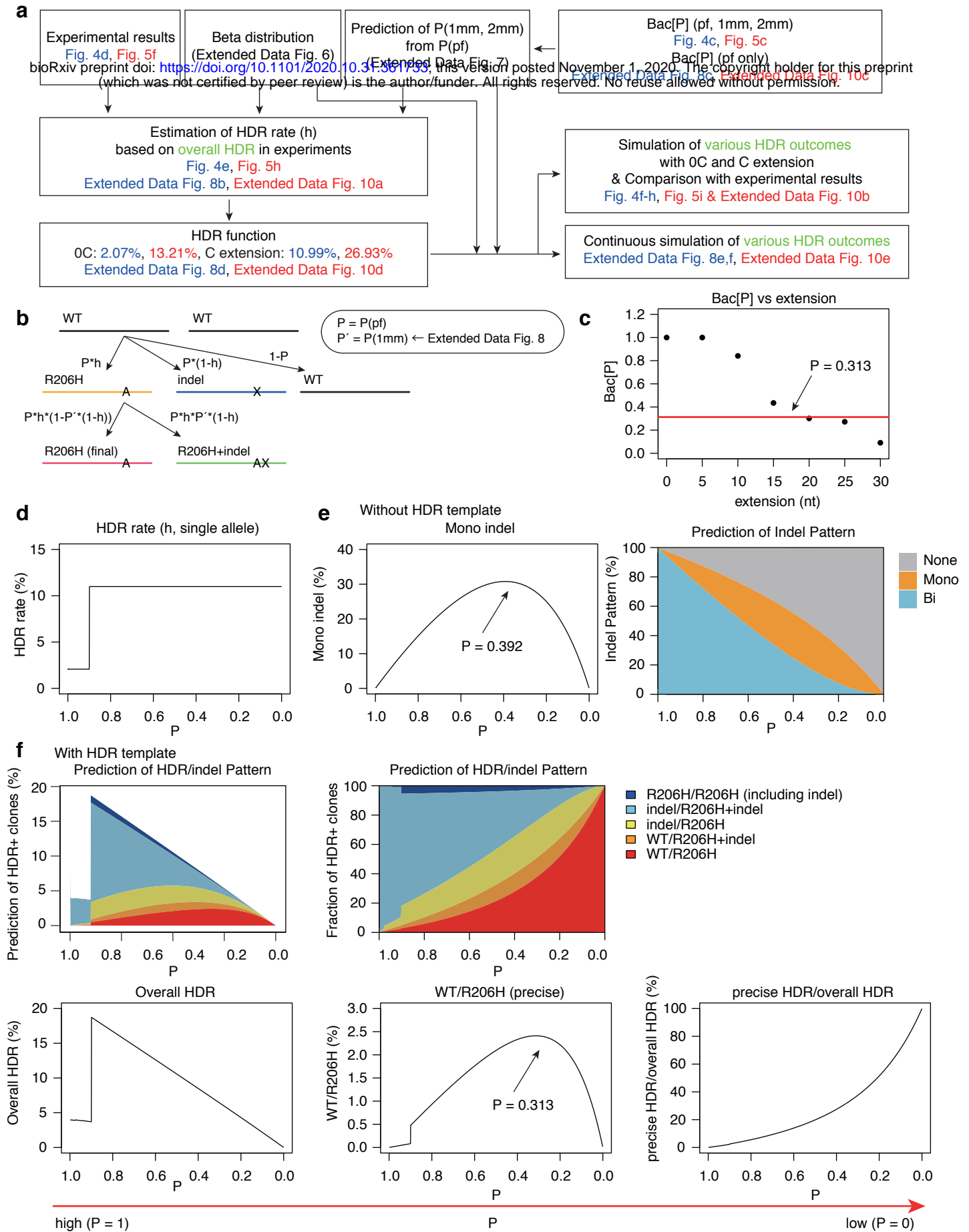
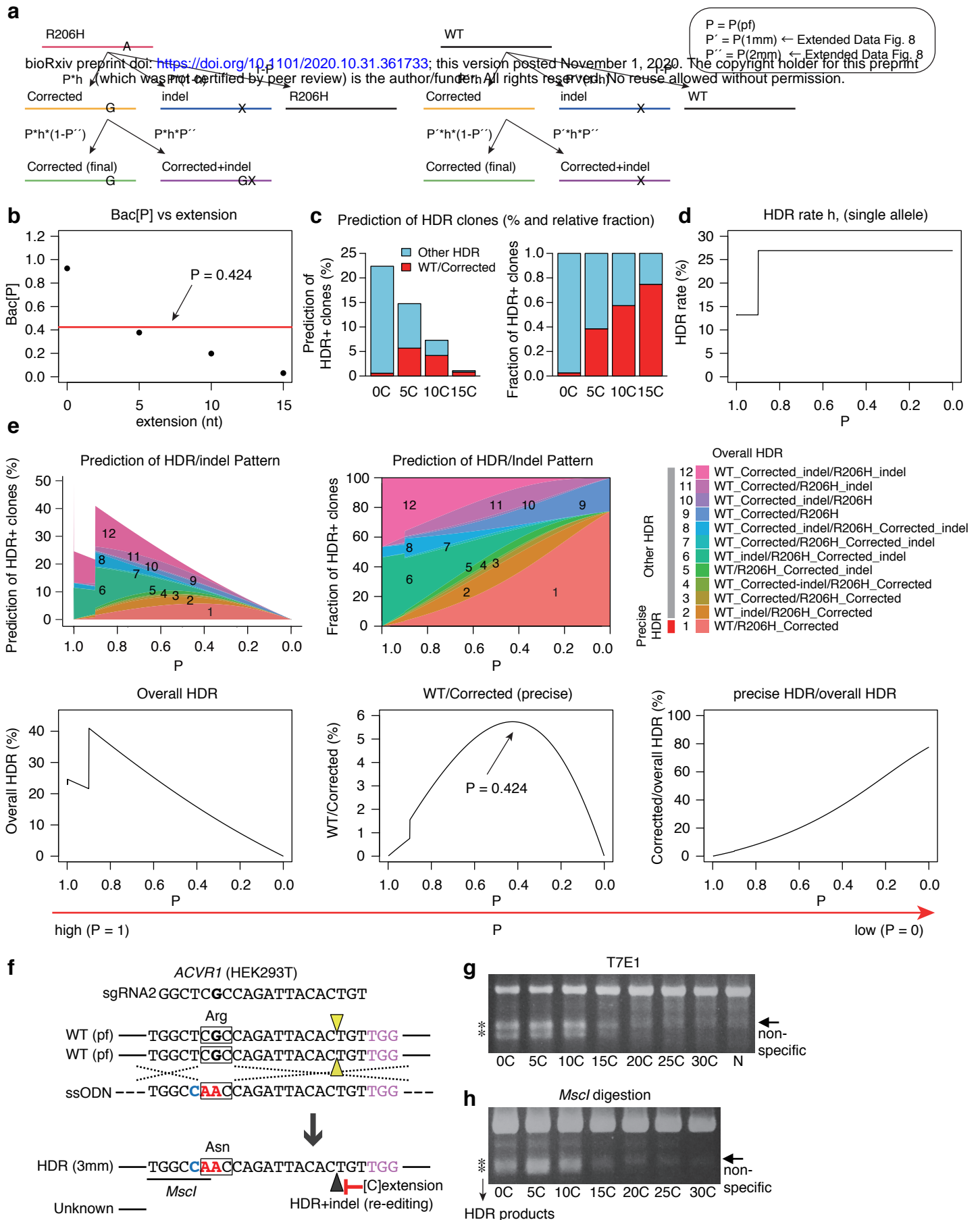**Extended Data Fig. 8. Computational simulation of precise mono-allelic HDR from homozygous states.**
a, A flow chart to establish a computational simulation of precise mono-allelic HDR to generate FOP model in mESC (Fig. 4 and Extended Data Fig. 8) or to correct a SNP in FOP hiPSCs (Fig. 5 and Extended Data Fig. 10). **b,** Scheme of HDR-mediated generation of FOP model (WT/R206H) from a WT/WT genotype. **c,** Relationship between [C] extension length and Bac[P] shown in Fig. 4c. A red line (P = 0.313) indicates the value when precise WT/R206H HDR is induced at the highest level. **d,** Hypothetical function of HDR rate (h) along indel probability (P). HDR rate is set based on the data of Fig. 4e (see details in Methods). **e,** Simulation of editing outcomes in the absence of HDR templates. Left and right panels show the relationships between indel probability (P) and frequencies for mono-allelic indel (left) or No/Mono/Bi indel (right). An arrow indicates the predicted maximum value for mono-allelic indel induction with P value of 0.392. **f,** Simulation of editing outcomes in the presence of HDR templates. Top panels show the relationships between indel probability (P) and frequencies of various HDR clones (top, left) and relative fraction (top, right). Frequencies of overall HDR and precise WT/R206H editing and the relative ratio of the WT/R206H clones (vs overall HDR) are shown in bottom panels. An arrow indicates the predicted maximum value (P = 0.313) to generate precise WT/R206H HDR clones.
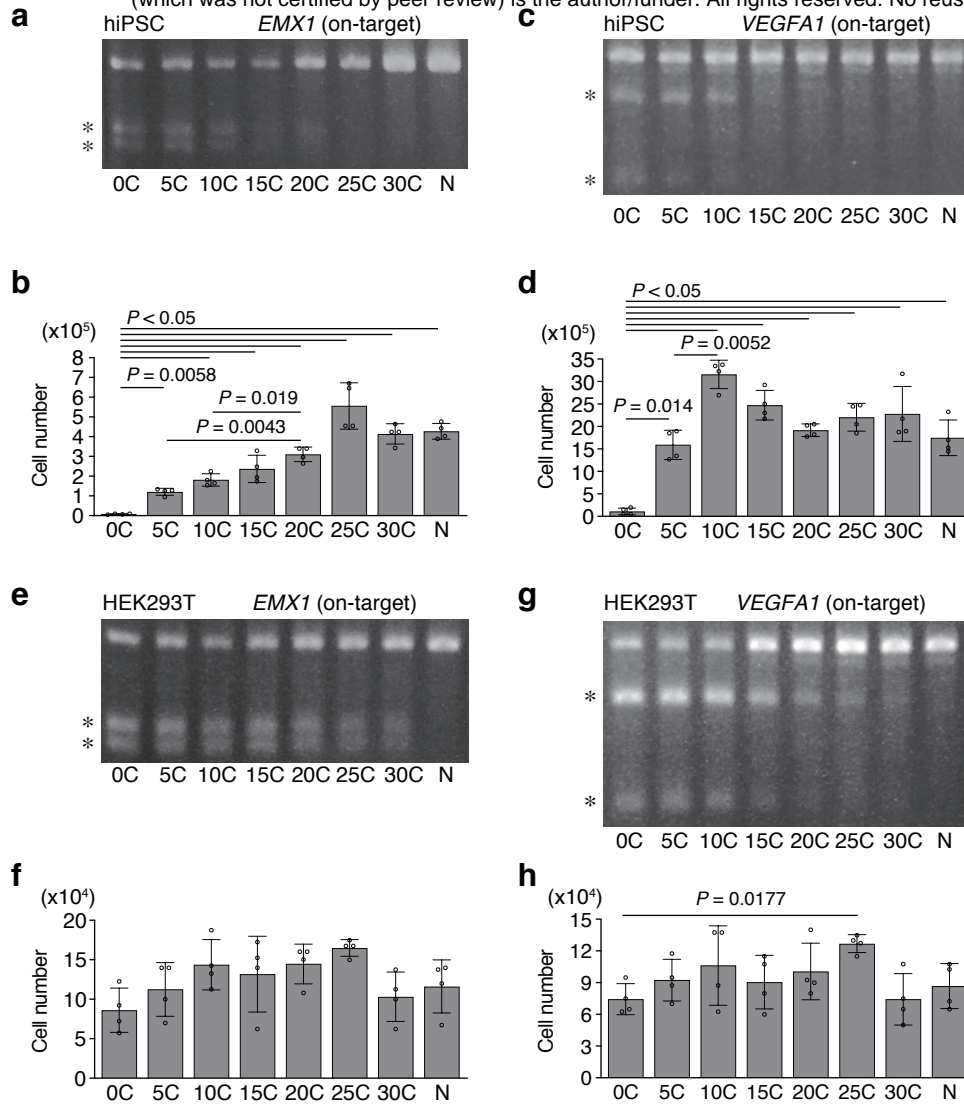
Extended Data Fig. 9. Suppression of cytotoxicity by [C] extension in hiPSCs.

a-d, Indel probability (**a, c**) and cytotoxicity (**b, d**) of other sgRNAs are investigated in hiPSCs. The T7E1 assay is performed to investigate on-target indel probability for sgRNAs targeting *EMX1* (**a**) and *VEGFA1* (**c**). These pictures are also shown in the Extended Data Fig 5c. **e-h,** Indel probability (**e, g**) and cytotoxicity (**f, h**) are investigated in HEK293T cells. The T7E1 assay is demonstrated to investigate on-target and off-target indel probability for sgRNAs targeting *EMX1* (**e**) and *VEGFA1* (**g**). These pictures are also shown in the Extended Data Fig 7c, d. N, PX459 plasmid without spacer (**a-h**). Asterisks indicate PCR products digested by the T7E1 assay (**a, c, e, g**). Statistical significance is assessed using Welch's test with post hoc Games–Howell test (**b, d, f, h**).

Extended Data Fig. 10. Computational simulation of precise disease gene correction.
a, Scheme of HDR-mediated correction of FOP model (WT/R206H) to a WT/Corrected genotype. **b,** Relationship between [C] extension length and Bac[P] for R206H allele, shown in Fig. 5c. A red line (P = 0.424) indicates the value when precise WT/Corrected HDR is induced at the highest level. **c,** Prediction of precise WT/Corrected clones and other HDR clones (left) and relative fraction (right). **d,** Hypothetical function of HDR rate (h) along indel probability (P). HDR rate is set based on the data of Fig. 5h (see details in Methods). **e,** Simulation of a relationship between indel probability (P) and various HDR outcomes (top, left) and relative fraction (top, right). Frequencies of overall HDR and WT/Corrected HDR and the relative ratio of the WT/Corrected clones (vs overall HDR) are shown in bottom panels. An arrow indicates the predicted maximum value (P = 0.424) to generate precise WT/Corrected HDR clones. **f-h,** Measuring HDR frequency in HEK293T cells. Schematic of HDR for 3 bp substitution in exon 5 of *ACVR1* (**f**). Silent mutation with cytosine (C, blue) and missense mutations with two adenines (AA, red) creates a *MscI* restriction enzyme site, which allows for rapid quantification of HDR frequency. Squares indicate codon. pf, perfect match; 3mm, 3 bp mismatches. Arrowheads indicate DSB sites. Asterisks indicate PCR products digested by T7E1 (**g**) or digested by *MscI* restriction enzyme (**h**). N, PX459 plasmid without spacer.